Pacific Northwest
National Laboratory

Operated by Battelle for the
U.S. Department of Energy

Evaluation of Scaling Correlations for Mobilization of Double-Shell Tank Waste

A. Shekarriz
K. J. Hammad
M. R. Powell

September 1997

Prepared for the U.S. Department of Energy
under Contract DE-AC06-76RLO 1830

Pacific Northwest National Laboratory
Richland, Washington 99352

PNNL-11737

PACIFIC NORTHWEST NATIONAL LABORATORY
operated by
BATTELLE
for the
UNITED STATES DEPARTMENT OF ENERGY
under Contract DE-AC06-76RLO 1830
Original Report Printed in the United States of America
Available to DOE and DOE contractors from the
Office of Scientific and Technical Information, P.O. Box 62, Oak Ridge, TN 37831;
prices available from (615) 576-8401
Available to the public from the National Technical Information Service,
U.S. Department of Commerce, 5285 Port Royal Rd., Springfield, VA 22161

PNNL-11737

Evaluation of Scaling Correlations for Mobilization of Double-Shell Tank Waste

A. Shekarriz
K. J. Hammad
M. R. Powell

September 1997

Prepared for the U.S. Department of Energy
under Contract DE-AC06-76RLO 1830

Pacific Northwest National Laboratory
Richland, Washington 99352

Executive Summary

In this report, we have examined some of the fundamental mechanisms expected to be at work during mobilization of the waste within the double-shell tanks at Hanford. The motivation stems from the idea that in order to properly apply correlations derived from scaled tests, one would have to ensure that appropriate scaling laws are utilized. Further, in the process of delineating the controlling mechanisms during mobilization, the currently used computational codes are being validated and strengthened based on these findings.

Experiments were performed at 1/50-scale, different from what had been performed in the previous fiscal years (i.e., 1/12- and 1/25-scale). It was anticipated that if the current empirical correlations are to work, they should be scale invariant. The current results showed that linear scaling between the 1/25-scale and 1/50-scale correlations do not work well. Several mechanisms were examined in the scaled tests which might have contributed to the discrepancies between the results at these two scales. No deficiencies in the experimental approach and the data were found. Cognizant of these results, it was concluded that the use of the current empirical correlations for ECR should be done cautiously taking into account the appropriate properties of the material for yielding.

To better understand some of the fundamental mechanisms within the "separate-effect" processes during mobilization, theoretical analysis was carried out, supported by careful laboratory measurements of turbulence within Newtonian and non-Newtonian jets. It was concluded that most of the mechanisms related to scaling of turbulent Newtonian jets and pseudoplastic jets are considered to be unimportant. It was found that as long as geometric scaling was properly maintained, the fluid did not develop *any* yield stress, and the jet Reynolds numbers were maintained above 10,000, then the dynamics within the jets scaled well. However, the jet turbulence studies were performed from a normal jet - sludge interaction point of view. It was concluded that the reason the 1/50-scale and 1/25-scale (and perhaps 1/12-scale) results did not scale was because of off-normal jet - sludge interactions. We do not believe that the material property variance played a significant role in the scaled experiments. Once the effect of off-normal interaction is included, then the results from various scales should collapse onto a unique set of curves.

Contents

Figures

Tables

1.0 Introduction

Numerous reports have been written on the strategy for mobilization of the settled sludges and mixing of the wastes in the double-shell tanks (DSTs) at the Hanford site. An overview of some of these studies and a historical perspective can be found in a recent report by Powell et al. (1997). In general, two groups of studies have been performed: computational, which simulates the conditions at the full-scale and reports the results of parametric studies; and experimental, where the mobilization of the waste at the full-scale is simulated at smaller, more practical scales and the results are scaled up to predict the conditions at full-scale. Although the question of validation of the computational models is important and one that is currently being addressed, we are more concerned in this report with how well the scaling laws have been utilized in the interpretation of the scaled experiments. Therefore, rather than an exhaustive review of the contents of many of these reports, we opt to focus on scaling and how to best implement it.

Mobilization and mixing of the double-shell tank (DST) sludges is comprised of several processes. The four most significant processes in chronological order, as shown in Figure 1.1, are: 1) growth rate or mixing ability of the jet (jet turbulence), 2) interaction of the jet with the sludge boundary, 3) erosion or failure of the sludge, and 4) removal and possible dissolution of the solids after erosion or failure. It is currently widely accepted that from the stand-point of complexity, these problems each embody many challenges in the area of hydrodynamics, aqueous phase chemistry, colloidal and interfacial science, and rheology, all working together during waste retrieval. To properly simulate the conditions anticipated during mobilization requires that many of the dominant scaling laws be satisfied.

While aqueous phase chemistry and colloidal science play an important role during retrieval, their effects will be captured in the macroscopic properties that affect mobilization and mixing. That is, during mixing, it is important to know which one of the species will go into solution (or precipitate) and the resulting influence on the solids content and size distribution as well as the rheological characteristics of the mixture (Onishi and Hudson 1996, Onishi et al. 1996, Smith et al. 1997). Once the properties are known or predicted then scaling can be approached from a purely mechanics point of view.

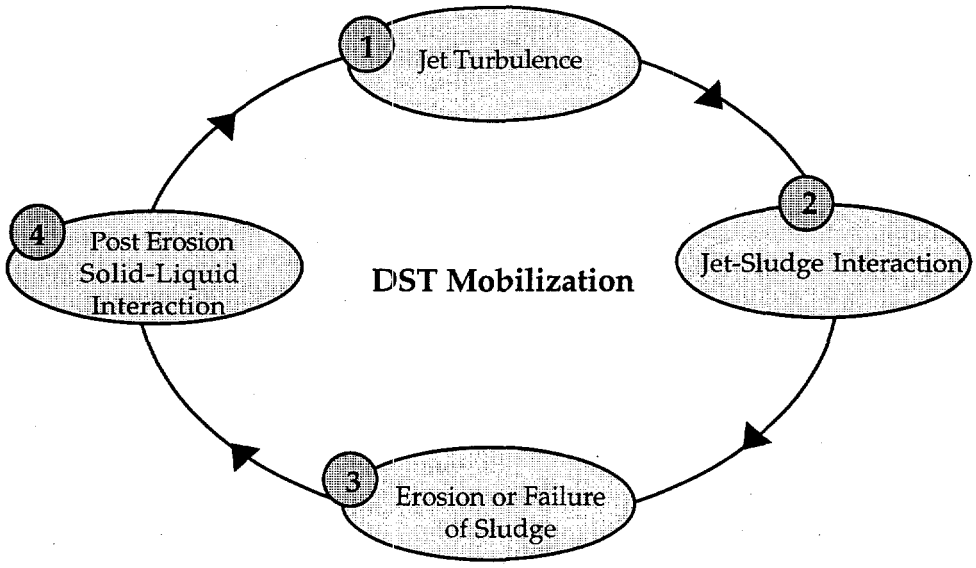

Figure 1.1. The Separate Effects Processes Involved in the Mobilization Phase of DST Retrieval

Most of the experiments that have been performed so far have lumped together all the processes described above in simulating the full-scale mobilization conditions. The significance of scale-up has been recognized in almost all the experimental work performed at the Pacific Northwest National Laboratory (e.g., Fort et al. 1993, Powell et al. 1995).[1,2] The dynamic, kinematic, and geometric scaling have in most cases been attempted through matching the Reynolds number, Froude number, Strouhal number, and tank and nozzle geometry (Powell et al. 1997).[1] However, most of the effort has been invested in the integrated rather than separate processes, what is known as "separate effects" experiments. Indeed if scaling is to hold in the "lumped effects" experiments, it should definitely hold in the separate effects experiments. Scaling is sometimes more challenging to achieve at the integrated level.

In one of the few separate effects experiments performed so far, Shekarriz et al. (1995a) showed that the rheology of the fluids used in a jet can affect the growth rate of the jet (i.e., the first process). Other separate effects experiments, for example, are the rheological studies performed in the laboratory to study how dilution changes the fluid rheology during retrieval;

---

[1] Bamberger, JA, LM Liljegren, and PS Lowery. December 1990. *Strategy Plan: A Methodology to Predict the Uniformity of Double-Shell Tank Waste Slurries Based on Mixing Pump Operation.* Unpublished PNL Report, Pacific Northwest Laboratory.

[2] Powell, MR,CL Flow, GA Whyatt, PA Scott, and CM Ruecker. November 1990. *Proposed Test Strategy for the Evaluation of Double-Shell Tank Sludge Mobilization.* Letter Report for Westinghouse Hanford Company, Pacific Northwest Laboratory.

i.e., the fourth process (Smith et al. 1997). In the following sections, we will discuss these processes in more detail.

1.1 Jet Turbulence

Bamberger et al.[3] provide a good review of the literature on post-mobilization mixing, or waste uniformity.[4] They found some insightful results in the literature for the relationship between mixing time in a stirred vessel (propelled) and Reynolds number. Van de Vusse (1955) found that in an unbaffled vessel, the mixing time of two stratified liquids with different densities decreases as a function of Reynolds number and reaches an asymptotic limit at $Re \sim 10^5$ beyond which it becomes a constant. The asymptotic limit correlation was found to be as shown below:

$$\theta \equiv \frac{T_m Q}{V} \approx 9\, Fr^{-1/4} \tag{1.1}$$

In the above equation θ is the dimensionless mixing time, T_m is the mixing time (*sec*), Q is the volumetric discharge of the jet or the impeller (m^3/s), V is the tank volume (m^3), and Fr is the Froude number defined as:

$$Fr \equiv \frac{\rho_l N^2 D^2}{\Delta\rho\, g\, H} \tag{1.2}$$

where ρ_l is the density of the liquid (kg/m^3), N is the rotation rate of the propeller ($1/s$), D is the propeller diameter (m), $\Delta\rho$ is the density differene between the two liquids (kg/m^3), g is the gravitational constant (9.81 m/s^2), and H is the height of the liquid in the tank (m). Norwood and Metzner (1960) found qualitatively similar behavior for baffled vessels. The asymptotic

---

[3] Bamberger, JA, LM Liljegren, and PS Lowery. December 1990. *Strategy Plan: A Methodology to Predict the Uniformity of Double-Shell Tank Waste Slurries Based on Mixing Pump Operation.* Unpublished PNL Report, Pacific Northwest Laboratory.

[4] This probelm is very similar to the mobilization problem with the exception of processes 2 and 3 which are less relevant or non-existent.

limit was reached at $Re \sim 10^4$ and at this limit the mixing time was a function of $Fr^{1/6}$ rather than $Fr^{1/4}$. The important result in both these studies is that at the limit of $Re \rightarrow \infty$, the dimensionless mixing time becomes only a function of Froude number and independent of Reynolds number.

It has also been noted that things are somewhat different when a jet is used for mixing of the liquid-liquid system.[5] Two different sets of results were found in this case. Fosset and Prosser (1951) performed experiments in 25 different large tanks with diameters ranging between 4.6 *m* and 44 *m*. They found that the asymptotic limit showed no Reynolds number dependence similar to the stirred vessel results disscussed earlier. However, when Fox and Gex (1956) performed similar experiments in smaller tanks ranging between 0.33 *m* to 4.6 *m*, they reported that beyond the transition Reynolds number of 2000, the dimensionless mixing time reaches an asymptotic condition which is a function of Reynolds number.

$$\theta \equiv \frac{T_m U_o D_o^{\,2}}{H D^2} \propto \left(\frac{Fr}{Re}\right)^{1/6} \tag{1.3}$$

where U is the velocity, the subscript o refers to the nozzle exit conditions, and the Reynolds and Froude numbers are based on the nozzle exit velocity and diameter. The proportionality was found to hold over essentially two orders of magnitude, up to $Re \sim 10^5$. Figure 1.2 is the summary of their results which shows the asymptotic conditions for a turbulent versus laminar Reynolds numbers.

Naturally, one would ask the following question: Is there a Reynolds number dependence? Indeed this is an important question that needs to be addressed. If there is no Reynolds number dependence, then as long as the different scaled experiments are operating at the asymptotic limit (say beyond $Re \sim 10^4$), then matching the Reynolds number at these different scales is not necessary. However, if the mixing time becomes a function of Reynolds number, then the Reynolds number at all different scales, in addition to other relevant dimensionless groups mentioned above, must be matched.

---

[5] Bamberger, JA, LM Liljegren, and PS Lowery. December 1990. *Strategy Plan: A Methodology to Predict the Uniformity of Double-Shell Tank Waste Slurries Based on Mixing Pump Operation.* Unpublished PNL Report, Pacific Northwest Laboratory.

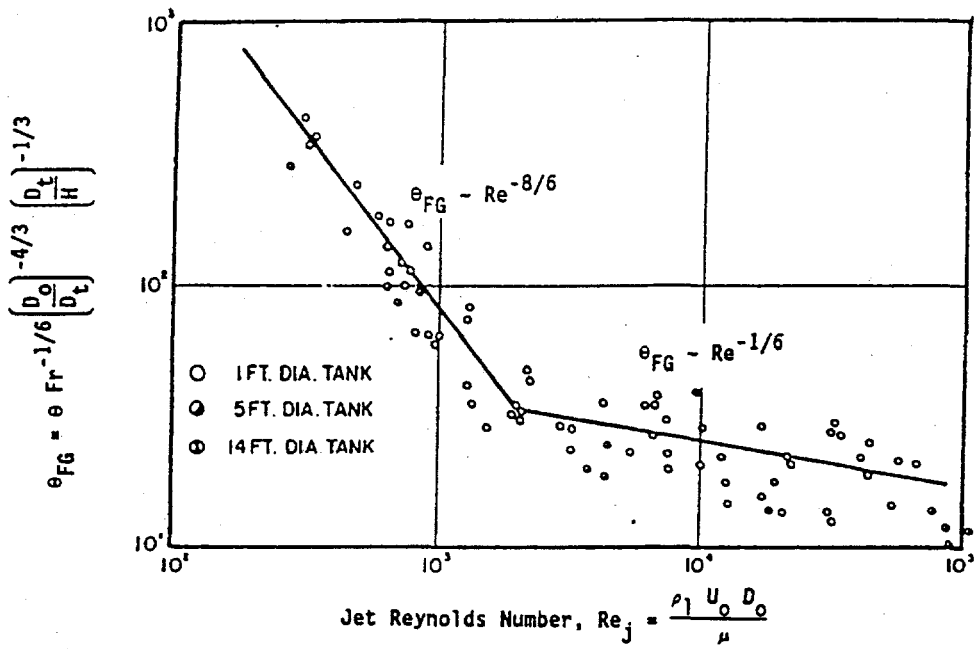

Figure 1.2. Jet Mixing of Liquids in an Enclosed Vessel (Fox and Gex 1956)

1.2 Jet-Sludge Interaction

To satisfy the laws of similitude in the form of dimensionless groups in this process (or any of the other processes), the flow generated at the sludge boundary, at which point erosion or failure of the sludge is taking place, would have to be independent of the scale of flow. Indeed similitude is easily demonstrated at very low Reynolds number conditions (Creeping flow) where once geometric similitude is satisfied, the streamlines in the flow at various scales, normalized by the scale of the system, collapse into a single set of streamlines (e.g., see White 1986). However, at higher Reynolds numbers, the flow becomes unsteady and randomly fluctuating[6] and highly unlikely to follow any similitude law on an *instantaneous* basis. When time-averaged, provided that the averaging time is larger than any inherent unsteadiness in the flow, the equations of motion provide several new sets of dimensionless groups which need to be satisfied to achieve similitude (e.g., see Schlichting 1960). Again the presumption is that the long-time asymptotic conditions are repeatable based on the issues governed by stability of nonlinear systems(e.g., see White 1974). Given slightly different input conditions, the system could seek a new equilibrium condition. But for all practical purposes, it is always assumed

[6] Although the idea of turbulent flows being deterministic has been contemplated, the current authors chose to look at turbulence as a stochastic process.

that the long-time asymptotic condition is always the same. However, there are instances where stochastic resonances can occur which amplifies one of the frequencies of unsteadiness in the flow field and if this resonance frequency happens to be very low (and commonly very energetic), then reaching a steady-state, long-time asymptotic condition becomes difficult.

Given the argument provided above, one can achieve full similitude (geometric, kinematic, and dynamic) after satisfying all the dimensionless groups that come out of the time-averaged turbulent flow equations and after long-time asymptotic conditions are reached at various scales.

To be more specific, there are two extreme steady-state conditions that can be considered for the interaction of the jet with the sludge boundary during mobilization: 1) pure shear interaction where the jet is moving parallel to the sludge interface and 2) stagnation flow interaction where the jet is impinging on the sludge interface at a normal incidence angle. In reality, the interaction of the jet and sludge may be somewhere in between the two. Powell et al.[7] have discussed these two scenarios (bulk erosion in normal incidence and erosion in parallel mode of interaction). The two relations that they propose, when properly derived in dimensionless format, appear as the following equations for the effective cleaning radius (ECR):

$$\text{Normal Incidence:} \quad \text{ECR}^* \equiv \text{ECR}/D = C_N \left(\tau_N / \rho U_o^2\right)^{-1/2} \tag{1.4}$$

$$\text{Parallel Interaction:} \quad \text{ECR}^* = C_P Re_D^{-2/5} (\tau_P / \rho U_o^2)^{-1/2} \tag{1.5}$$

where Re_D is the Reynolds number based on the nozzle diameter and the nozzle exit velocity and the fluid viscosity in the jet, C_N and C_P are empirical constants found experimentally, and τ_N and τ_P are the yield strength in the normal and parallel failure modes. Of course, it is implicitly implied in the above relations that the fluid remains Newtonian throughout the flow field and that turbulence in the jet is similar to what is reported for a turbulent Newtonian free jet (see, for example, Rajaratnam 1976).

A surprising result that has not been elaborated in the previous reports is that the

---

[7] Powell, MR,CL Flow, GA Whyatt, PA Scott, and CM Ruecker. November 1990. *Proposed Test Strategy for the Evaluation of Double-Shell Tank Sludge Mobilization.* Letter Report for Westinghouse Hanford Company, Pacific Northwest Laboratory.

relation between ECR and the shear strength remains the same regardless of the orientation of the jet with respect to the sludge interface. The minimum requirement for this relation to be true is that the modes of failure in both cases have to be the same and the parameter that represents the material erosion or failure is the shear strength, τ_s. As a first order investigation, Powell et al. (1995) characterized several different sludge simulants using different instruments that are likely to fail the material in different modes (i.e., yield stress using a parallel plate rheometer and shear strength using a shear vane). They found that the ratio of the shear strength to yield stress was nearly a factor of two for all the different sludges tested. Thus, for all practical purposes, the functional dependence of ECR on the shear strength is as shown in Equations (1.4) and (1.5) and the same for both modes of erosion. (More on this topic will be covered in the following section.)

A more important issue is that in the normal mode of erosion (Equation(1.4)), ECR is independent of the Reynolds number. However, similar to what is shown graphically in Figure 1.3, the parallel incidence mode results in erosion which depends on the Reynolds number. Thus, as the Reynolds number goes up, the ECR decreases. This is an important issue which will be taken up again throughout the remainder of this report.

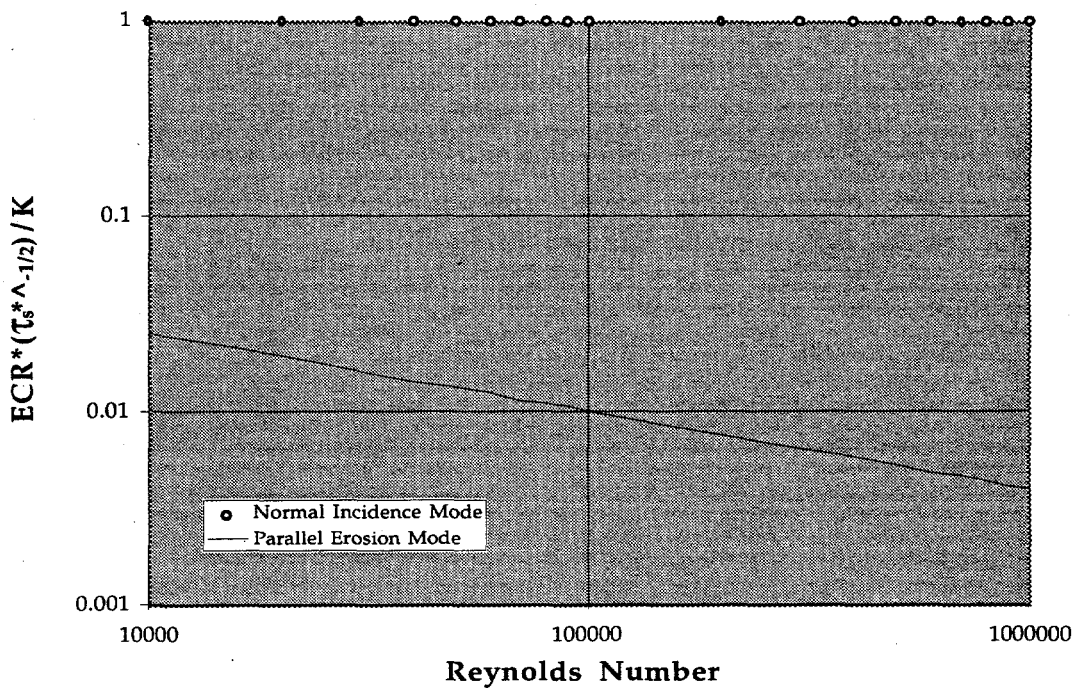

Figure 1.3. Dependence of ECR on Reynolds Number for the Parallel and Normal Jet-Sludge Interaction Modes.

1.3 Erosion or Failure of Sludge

This particular process is one that is currently in the process of evaluation. The biggest question in this area is whether or not to treat a cohesive sludge as an elastic solid or a solid-liquid slurry. Observations reveal that a cohesive slurry can fail in bulk possibly along slip planes like a solid material (Powell et al. 1995). It is expected that the higher the interaction force between the particles, the higher will be the tendency for the material to fail or fracture like a solid. For all practical purposes, we can then treat the waste as a solid material prior to mobilization since in most cases the sludges have finite strengths that can be as high as ~10^4 *Pa*, certainly in the compressive mode of failure (Onishi et al. 1996).

From a stand-point of failure of a solid material, there is a lot that is known about the subject. There are different failure theories and criteria that can be adopted. e.g., Maximum Stress Principle and Minimum Energy Principle (Beris et al. 1985). In general however, failure occurs along the axis of principle stresses and can be aligned in the pure shear direction, pure normal stress direction (tensile or compressive), or anywhere in between. As long as the solid deforms within the Hookean linear elastic regime, then the ratio of the compressive yield stress, τ_c, and shear yield stress, τ_s, may be written as shown below:

$$\frac{\tau_c}{\tau_s} = \frac{2(1-\epsilon)}{1-2\epsilon} \tag{1.6}$$

where ϵ is the Poisson's ratio. For solids, the Poisson's ratio is ~0.3 and Equation (1.6) suggests that the compressive yield stress should be ~4 times the shear yield. Studies on aggregated suspensions (Channell and Zukoski 1997) suggest that suspensions which develop a structure behave very similar to a solid. The Poisson's ratio for these suspensions has been reported to range between 0.475 to 0.497 (Meeten 1994). Using Equation (1.6), the compressive yield of these suspensions would then be approximately 21 to 168 times higher than the shear yield. Channell and Zukoski (1997) found that the alumina suspensions in their study produced a ratio of approximately 55 between the two yield strengths.

Powell et al. (1995) measured the (shear) yield stress and the tensile strength of several different mixes of bentonite and kaolin clays. The yield stress was measured using a rotational viscometer and the tensile strength was measured using a tensiometer. They found that the

tensile strength was between 2 to 7 times higher than the yield stress. They also measured the shear strength of the same material using a shear vane rheometer and found that in most cases the shear strength was lower than the tensile strength but closer to the tensile strength than to the yield stress. Extensive measurements of the compressive yield strength are not available other than what is presented by Onishi et al. (1996). They found that the yield in the compressive mode for SY-102 sludge is approximately 8000 *Pa*. Using the above range of Poisson's ratios, the shear yield for the SY-102 sludge would be approximately 50 *Pa* to 380 *Pa*. This range of values is between 10 to 78 times lower than the shear strength measurements performed in the hot-cell using a shear vane instrument (DiCenso et al. 1995). The typical values of the yield stress for the DSTs when a ball rheometer was used are in the ~200 *Pa* range and consistent with the values based on the Poisson's ratio approximations (Stewart et al. 1996).

Onishi et al. (1996) also report a value of 2.7 *Pa* for the yield stress of the SY-102 waste. This measurement was performed in a hood with a rotational device using a cone-and-plate sensor. We believe that the sample was excessively disturbed and since the shear stress measurements are very sensitive to the sample disturbance, then the value of 2.7 *Pa* may be a gross underestimation of the shear yield of the material. Currently, we are continuing to determine what the modes of failure of the sludges in the tank are and whether or not parameters such as compressive yield stress is one of the material properties that plays a role in the failure modes of the sludges.

1.4 Post-Erosion Solid-Liquid Interaction

What we have attempted to provid in the previous sections, is a phenomeno-logical picture of the processes involved in the tank during the mobilization phase of retrieval. We started with the jet and what affects its characteristics. We discussed what happens downstream when the jet reaches the sludge bank and interacts with it and how it might fail or erode the sludge. In an enclosed environment, one would need to be concerned about what the mobilized solids might do to the "freestream" fluid properties. Including the effect of the changes in the supernatant liquid during mobilization essentially completes the loop of the processes that are important during the mobilization phase of DST retrieval.

Indeed if the ratio of the sludge volume to the total waste volume in a tank is not large, as for example would be the case in Tank AZ-101, then changes in the supernatant liquid

properties due to the addition of eroded solids is expected to be negligible. Under conditions where the sludge to total waste volume in a tank is high, such as in the AN tanks, or if the supernatant liquid is near or at saturation point with respect to some of the solids in the sludge layer, then the eroded solids would potentially change the characteristics of the supernatant liquid during mobilization. Some of these issues have been addressed by Onishi and Hudson (1996) where they performed modeling of dilution during mobilization using the computational chemistry code, GMIN. The computational approach in conjunction with an empirical approach based on laboratory and hot-cell measurements where phase equilibria studies can be performed would provide information about what chemical and as a result rheological changes can be expected in the supernatant liquid (or mixture) during mobilization.

Because of the tank-specific nature of this rather complex process, we will not include in this report any part of the process of post-erosion interactions between the liquid and eroded solids. Instead, we will assume an expected range of rheological characteristics of the supernatant liquid as an input from this process into the first process (Figure 1.1).

In the remainder of this report we will present some theoretical views toward scaling of turbulent free jets and wall jets (Section 2). In Section 3 we will present the results of the experiments performed to simulate the DST mobilization at 1/50-scale. We will compare these results to those obtained from 1/12- and 1/25-scale experiments. In Section 4 we will present the results that we have obtained so far on turbulence within Newtonian and non-Newtonian jets. Some of these results were obtained in the previous fiscal years with support from the DST Retrieval project, but were not published in a PNNL report. We will discuss our observations and present the conclusions in Section 5.

2.0 Turbulent Jets Scaling: Theoretical Approach

In this section, instead of progressing in a chronological order of events as we did in Section 1, we will start by focusing our attention on the inteface of the sludge when momentum and energy exchange between the jet and sludge are taking place. As mentioned in Section 1.2, the two extreme steady-state jet-sludge interactions are normal and parallel orientations. The mechanistic view of these interactions is described in Sections 2.1 and 2.3.

2.1 Purely Normal Interaction - Stagnation Flow

Consider the case where the jet impinges on the sludge interface at a normal incidence angle. The geometry of flow is depicted in Figure 2.1. If we assume that the jet is a turbulent Newtonian jet and the flow in the jet is not influenced by the presence of the sludge interface (one-way coupling), then the instantaneous force balance on the surface ($x=x_p$) along the x-axis can be written as:

$$\sum F_x = \int_A (\sigma_{xx} - \tfrac{1}{2}\rho u^2) \cdot dA = 0$$
$$\sigma_{xx} = \tfrac{1}{2}\rho u^2 \qquad (2.1)$$

where u is the instantaneous velocity at x_p, σ_{xx} is the instantaneous normal stress acting on the surface, and ρ is the density of the fluid. The instantaneous velocity in the jet can be presented in terms of the time-average axial velocity, $\bar{u}$, and the fluctuating component of the axial velocity, u'.

$$u \equiv \bar{u} + u'. \qquad (2.2.)$$

Substituting Equation (2.2) into (2.1) and by time-averaging the resulting equation we obtain the following relationship for the normal stress or pressure on the surface.

$$\bar{\sigma}_{xx} = \tfrac{1}{2}\rho(\bar{u}^2 + \overline{u'^2}). \qquad (2.3)$$

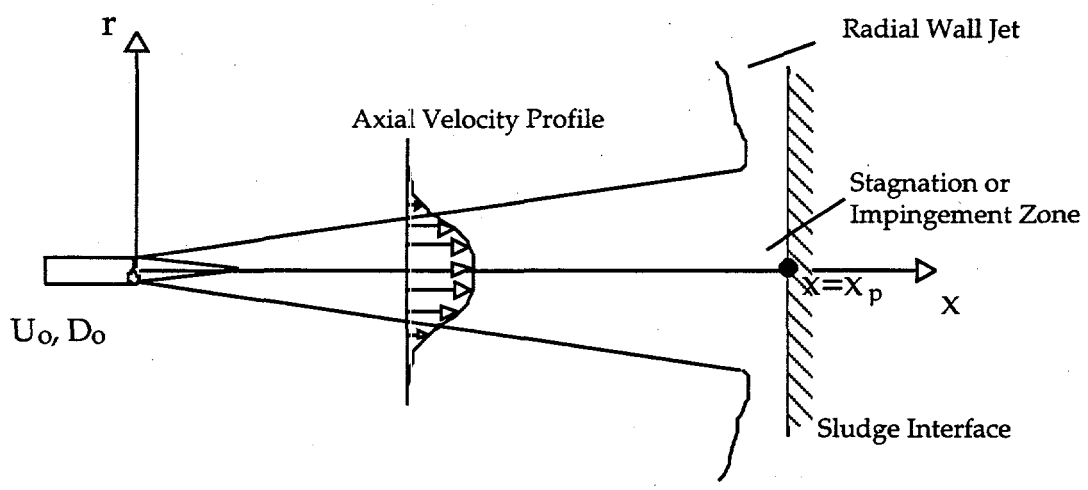

Figure 2.1. Schematic Diagram Depicting the Flow Geometry for the Normal Jet-Sludge Interface Interaction Mode

Indeed Equation (2.3) reveals that the slow time (or time-averaged) local pressure acting on the surface of the sludge is the sum of the mean kinetic energy of the flow and the turbulent kinetic energy. At the center, or $r=0$, where the stresses are maximum and where the failure is likely to be initiated, the ratio of the axial turbulent to mean kinetic energies has been reported to be approximately 8% for submerged water jets (Wygnanski and Fiedler 1969). Thus, we may re-write this equation by lumping the turbulent kinetic energy terms into the time-averaged term:

$$\bar{\sigma}_{xx} = C_1 \left(\tfrac{1}{2} \rho \bar{u}^2 \right) \tag{2.4}$$

or in a nondimensional format

$$\frac{\bar{\sigma}_{xx}}{\frac{1}{2}\rho U_o^2} = 42\, C_1 / (x/D)^2 \tag{2.5}$$

where the constant C_1 becomes a function of the flow conditions and can be determined empirically. At the limit when the jet acts like a turbulent Newtonian free jet, C_1 approaches

1.08 in the center of the jet.[8] However, when placed in an enclosure of finite size, such as in the tanks of limited volume, the parameter C_J might exhibit some dependence on the Reynolds number and the tank dimensions. This is an issue which has been verified in this study and will be discussed in Sections 2.4 and 4.0. Now, if Equation (2.4) is used in the derivation of an ECR relation similar to Equation (1.4), then the parameter C_N would include C_J and its dependence on Reynolds number and scale of the system would have to be verified.

2.2 Purely Shear Interaction - Wall Jet Flow

The problem of turbulent wall jets degenerates into a number of different problems each yielding a unique solution. Rajaratnam (1976) provides a comprehensive review of the literature and some of the closed-form solutions found for wall jets. Figure 2.2 is a schematic diagram depicting the geometry of flow for a plane or circular wall jet. The elevation between the jet and the wall is ignored in this case. It has been shown that for this problem, as the velocity develops in the downstream direction, the profile of velocity becomes similar beyond x/D~20. The similar velocity distribution for a plane wall jet takes on the form shown below:

$$u/u_m = 1.48\,\eta^{1/2}\left[1 - erf(0.68\,\eta)\right] \tag{2.6}$$

where u_m is the maximum velocity at each axial location (x), η is the dimensionless position normal to the wall, y/b, and b is the width of the jet. The wall shear stress can be obtained from Equation (2.6) from differentiation with respect to y at the wall.

$$\bar{C}_f \equiv \frac{\bar{\tau}_{yx}}{\rho U_o^2/2} \simeq 0.2\,(x/D)^{-1} Re_D^{-1/2}. \tag{2.7}$$

---

[8] Beltaos and Rajaratnam (1974) have shown that the pressure at this point is approximated as:

$$\bar{\sigma}_{xx}/(\frac{1}{2}\rho U_o^2) \simeq 50/(x/D)^{-2}.$$

This equation results in a slightly higher pressure than what is shown in Equation (2.5). But for all practical purposes, it follows the same scaling relations as (2.5).

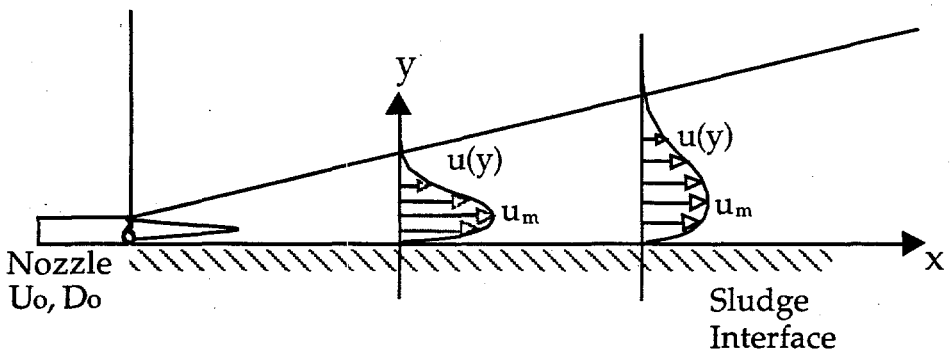

Figure 2.2. Flow Geometry for the Parallel Jet-Sludge Interface Interaction Mode (Wall Jet)

In the above equation, $\bar{\tau}_{yx}$ is the time-averaged wall shear stress and $\bar{C}_f$ is the dimensionless shear stress or skin friction coefficient. The form of the skin friction coefficient remains approximately the same for a radial wall jet produced by an impinging circular jet, as shown in Figure 2.1. Equation (2.7) indicates that the skin friction coefficient acting on the sludge decreases as Reynolds number increases.

One may use Equation (2.7) to predict the ECR for a parallel interaction. This can be done by noting that x=ECR when $\tau_{yx} = \tau_p$. As defined in Section, τ_p is the material yield strength in the parallel mode (shear yield). Thus find that Equation (2.7) provides the following relationship for estimating the ECR:

$$ECR/D \simeq 0.2\, Re_D^{-1/2} (\tau_p / \tfrac{1}{2}\rho U_o^2)^{-1}. \qquad (2.8)$$

In contrast to Equation (1.5), which was reported by Powell et al.,[9] Equation (2.8) shows an inverse relation between ECR and yield strength. Since Equation (2.8) was derived from the relationships reported for a wall jet, rather than a plane boundary layer flow, we consider this relationship to be more realistic.

---

[9] Powell, MR,CL Flow, GA Whyatt, PA Scott, and CM Ruecker. November 1990. *Proposed Test Strategy for the Evaluation of Double-Shell Tank Sludge Mobilization.* Letter Report for Westinghouse Hanford Company, Pacific Northwest Laboratory.

2.3 Combined Stress Interaction

In the previous two sections two limiting cases for the stresses acting on the surface of the sludge have been considered. At the one limit, where only normal incidence is considered, no dependence on the Reynolds number was found. On the other hand, when considering the parallel interaction or wall jet limit, then a dependence of $Re_D^{-1/2}$ was found. As mentioned before, the interaction in the actual flow conditions is likely to be a combined mode, somewhere between the two extreme conditions. Figure 2.3(a) is a schematic depiction of the stresses acting on the sludge interface when the incidence angle, α, is between 0 and 90°. Similar to our previous definitions, τ and p are the shear and normal stresses acting on the surface of the sludge.

$$\begin{aligned} p &= \bar{\sigma}_{xx} \sin \alpha \\ \tau &= \bar{\tau}_{yx} \cos \alpha \end{aligned} \tag{2.9}$$

$\bar{\sigma}_{xx}$ and $\bar{\tau}_{yx}$ are the time-averaged normal and shear stresses found in the previous two sections (Equations (2.5) and (2.7)). Figure 2.3(b) is the Mohr's circle representation of the stresses acting on the surface. The resultant stress at each point on the surface can be found from the following relationship:

$$\bar{\sigma}_R = [(\bar{\sigma}_{xx} \sin \alpha)^2 + (\bar{\tau}_{yx} \cos \alpha)^2]^{1/2} \quad . \tag{2.10}$$

Substitution of the Equation (2.5) and (2.7) into (2.10) results in the following relationship for the resultant wall stress.

$$\frac{\bar{\sigma}_R}{\frac{1}{2}\rho U_o^2} = [(\frac{42\, C_1}{(x/D)^2} \sin \alpha)^2 + (\frac{0.2\, Re_D^{-1/2}}{(x/D)} \cos \alpha)^2]^{1/2} . \tag{2.11}$$

Equation (2.11) can be used in estimating the effective cleaning radius, ECR, for the jet, similar to the approach used in the previous sections.

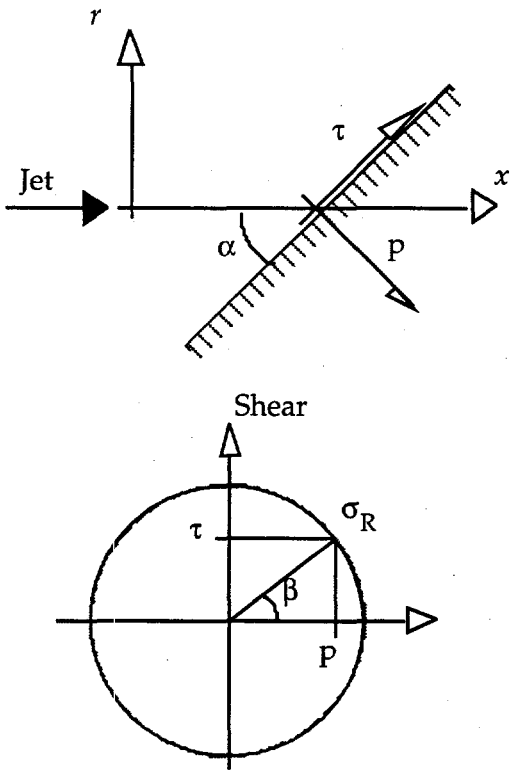

Figure 2.3. Geometry of Flow for Combined Stress Interaction

2.4 Effect of Enclosure on Jet Turbulence - Confined Jets

Most of the analysis performed in the previous sections (2.1 through 2.3) assumes that the jet can be modeled as a free jet. By definition, a free jet is produced when the flow out of a nozzle is issued into a quiescent freestream fluid. When a jet is placed in an enclosure with characteristic dimensions in the order of or smaller than the integral length scale of the jet,[10] then the jet is no longer free and it is considered as a confined jet.

Confined jets have been studied in the past due to their practical applications in jet pumps and furnaces. In these configurations, the fluid within the jet is propelling the surrounding fluid and as a result both fluids are flowing in the same direction (i.e., coflowing jets). However, if the initial momentum of the jet is sufficiently high, recirculation can take place within the channel in which the jet is issued. Turbulence measurements of Curtet and

---

[10] The simplest definition for the integral length scale is that it is the scale of the largest eddies found in a jet. This scale usually grows with the dimensions of the jet in the downstream direction.

Ricou (1964) and Barchilon and Curtet (1964) show that as the recirculation in the enclosure becomes more and more intense (e.g., by increasing the jet Reynolds number), the turbulent intensity (or kinetic energy of turbulence) increases above the measured free jet values. They found that when the jet velocity exceeded the average velocity in the enclosure by an order of magnitude or more, the turbulent intensity in the jet becomes more than 3 times higher than what is found in a free jet.

These results, however, are considered to be specific to the particular geometry they studied. The ratio of the confinement diameter to the diameter of the jet was 13.5 which is considerably smaller than the enclosures that we would be concerned about in our scaling analysis. Indeed an increase of 3 times on the turbulent intensity, which is equivalent to almost an order of magnitude increase in the turbulent kinetic energy, would make the turbulent kinetic energy as large as the kinetic energy of the mean flow (see Equation (2.3)). Thus, the extent to which the enclosure geometry plays a role is of high interest here.

To understand why the turbulent intensity within the jet increases when confined we will resort to a simple model for the jet. Figure 2.4 schematically shows the balance of the turbulent kinetic energy (TKE) on the jet control volume.

$$\Delta k_j = k_N + k_E - k_o \tag{2.12}$$

where,

$k_N \equiv$ TKE from Nozzle

$k_o \equiv$ TKE Leaving the Jet

$k_E \equiv$ Entrained TKE

$\Delta k_j \equiv$ Change in the TKE within the Jet

= Production of TKE − Dissipation of TKE.

Indeed, Equation (2.12) reveals that if the amount of the entrained TKE goes to zero, the TKE at any point in the jet is the summation of the net TKE produced within the jet and the inlet TKE coming from the nozzle. This limiting condition is essentially what exists in a free jet. However, what makes the confined jet unique is the entrained TKE, which we will call "TKE feedback."

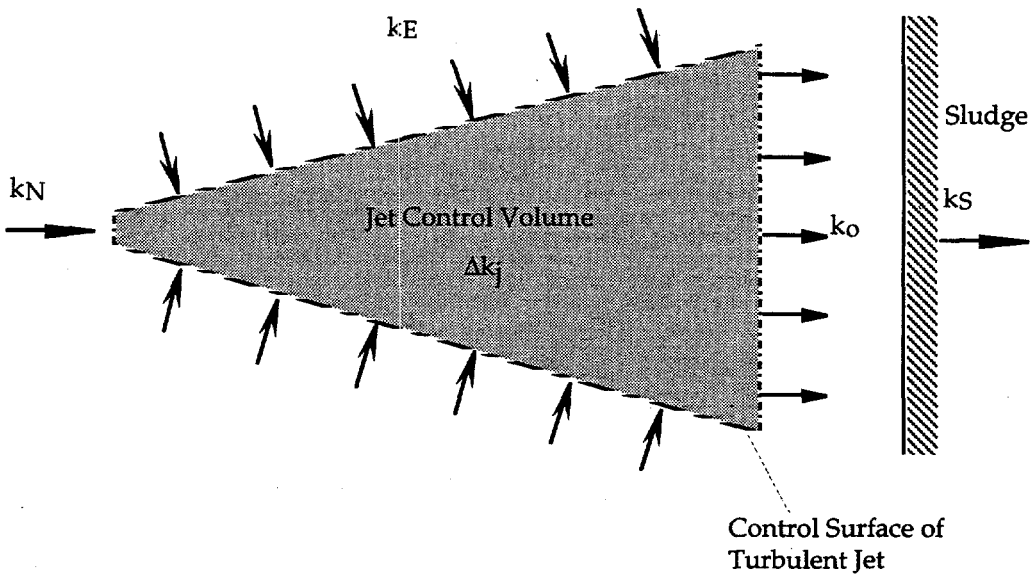

Figure 2.4. Turbulent Kinetic Energy Budget on the Jet Control Volume

The TKE leaving the jet, k_o, is linked to the TKE feedback, k_E, via the following relationship which holds within a finite enclosure.

$$\Delta k_R = k_o - k_E \tag{2.13}$$

where,

$\Delta k_R \equiv$ Change in the TKE within the Recirculation Zone.

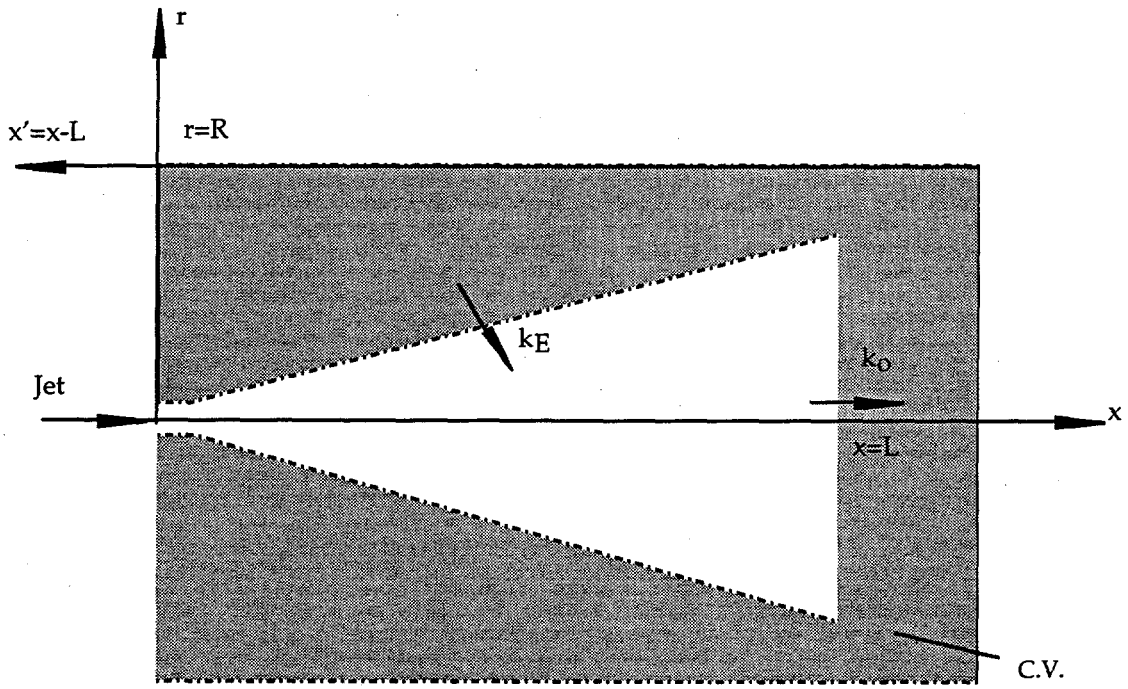

Figure 2.5. TKE Budget in the Recirculation Zone.

We recognize that the rate of change of the TKE within the recirculation zone is linked to the rate of dissipation of TKE. We will model the turbulence within this region as being homogeneous and isotropic.

$$\frac{dk_R}{dt} = \varepsilon(t) = 15\nu\frac{u_R^2}{\lambda^2}. \tag{2.14}$$

In Equation (2.14) the parameter u_R is the fluctuating component of the velocity within the recirculating zone. Indeed, k_R is linked to the square of the fluctuating component of velocity. While Equation (2.15) works well for a Newtonian fluid, its applicability in a non-Newtonian fluid is highly questionable. In general, we expect that the dissipation is higher when a shear thinning fluid is used because the recirculating flow becomes much more viscous and

dissipative. Further, the parameter λ is the integral length scale of turbulence for a Newtonian fluid, as defined earlier in this section. Tennekes and Lumley (1992) propose that the integral length scale can be quantified using the following relation:

$$\frac{\lambda}{\ell} = 15^{1/2}\, Re_{\ell}^{-1/2}. \tag{2.15}$$

In the above equation, Re is the Reynolds number of the flow within the recirculation zone and ℓ is an appropriate length scale of the system. Since we have two different length scales for characterizing the system, L and R, we postulate that the eddies can not get larger than the smaller of the two length scales. Hence, we will choose the smaller of the two scales in accordance with the following formula:

$$\ell \approx (1/L^2 + 1/R^2)^{-1/2}\ . \tag{2.16}$$

We also need to do a Taylor transformation between time and space according to the following relationship:

$$t = \zeta / U_R \tag{2.17}$$

where,

$\zeta \equiv$ Path Length of Recirculating Flow $= (x'^2 + r^2)^{1/2}$

$U_R \equiv$ Recirculation Velocity

Substitution of Equations (2.15) through (2.17) into Equation (2.14), solving for k_R, and using the boundary condition $k_R = k_o$ at $x' = 0$ (and $r = 0$) results in the following closed form solution for the variation of the TKE within the recirculation zone.

$$\frac{k_R}{k_o} = e^{-\frac{2}{3}\zeta/\ell} \tag{2.18}$$

where ζ and ℓ were defined previously in Equations (2.16) and (2.17). Equation (2.18) reveals that the TKE within the recirculation zone can be found from the knowledge of the initial TKE

entering the recirculation zone, k_o, and the geometry of the recirculation zone (or the container). It is through Equation (2.18) that we can determine the TKE feedback into the jet. We will assume that the TKE feedback is equal to k_R at $L/2$ and we substitute the resulting equation into Equation (2.12) and solve for k_o.

$$k_o = \frac{k_N + \Delta k_j}{1 - exp\left[-\frac{1}{3}\left(1+(L/R)^2\right)^{1/2}\right]} = \frac{k_{o,fj}}{1 - exp\left[-\frac{1}{3}\left(1+(L/R)^2\right)^{1/2}\right]}. \tag{2.19}$$

In the above equation, $k_{o,fj}$ is the TKE for a free jet. Note that although the integral length scale is a function of the Reynolds number or how fast the recirculation flow is driven, the final result shown in Equation (2.19) does not show any dependence of the jet turbulence on the Reynolds number.

Figure 2.6 is a graphical representation of the ratio of the confined jet to the free jet turbulence found from the above model. There is, however, dependence on the aspect ratio of the container, L/R, indicating that as the $L/R \rightarrow \infty$, then $k_o \rightarrow k_{o,fj}$ which is consistent with our intuition, since the return path for the recirculation is so long that the TKE dissipates entirely before it has a chance to re-entrain into the jet. At the other asymptotic limit where the $L/R \rightarrow 0$, the kinetic energy in the jet reaches a steady limit of 3.5 times the free jet turbulent kinetic energy.

Another observation in Equation (2.19) is that there is no dependence on the Reynolds number of the flow. This result is somewhat surprising since the literature cited earlier reveals that the TKE in a confined jet increases as the recirculation in the confinement becomes more and more intense. i.e., as the jet velocity increases. Equation (2.19) suggests that an increasing recirculation velocity results in an increase in the dissipation rate that counteracts the decreasing dissipation time. Thus no net change in the feedback TKE is obtained by changing the flow Reynolds number. Indeed this issue has been verified in the current study for a particular L/R ratio, as will be discussed in Section 4.0. But, we have found that for a Newtonian jet flowing within our particular confinement geometry, there was no measurable change in the TKE as a function of Reynolds number.

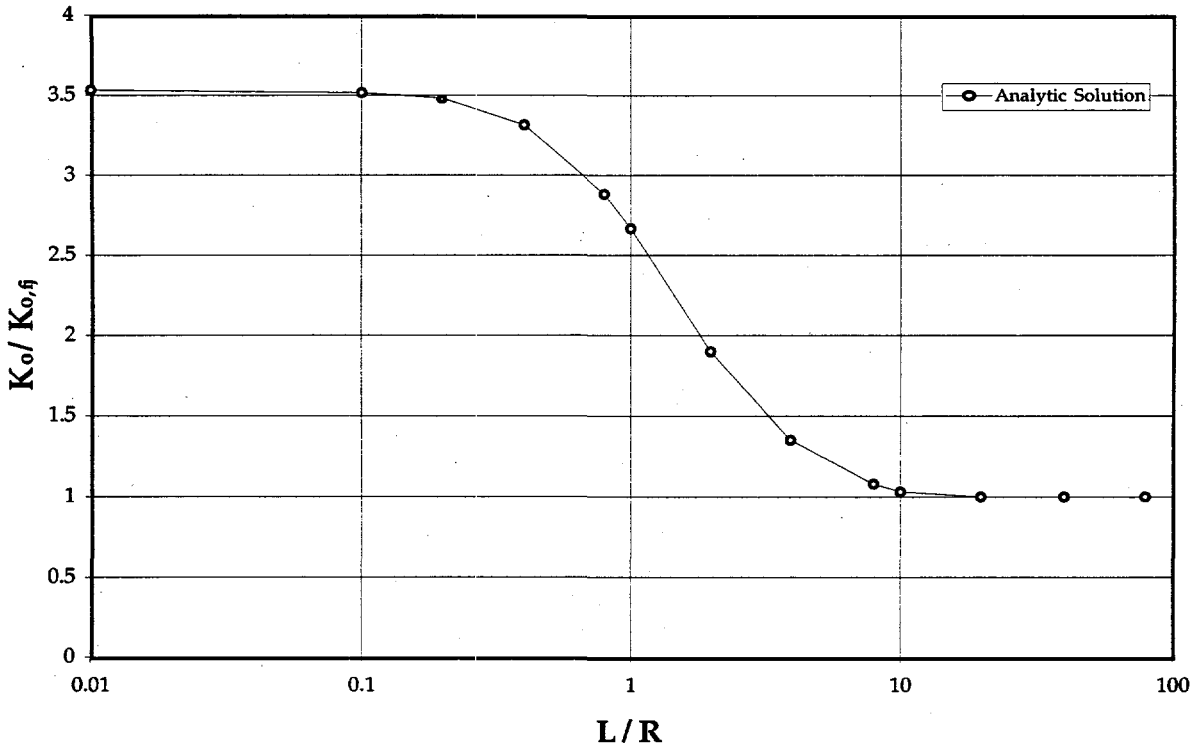

Figure 2.6. Ratio of Turbulent Kinetic Energy in a Confined Jet Versus a Free Jet.

2.5 Turbulent Non-Newtonian Jet

The behavior of pseudoplastic and yield-pseudoplastic jets has been of interest for many years because of their use for mixing and resuspension of settled slurries within industrial processes. Previous studies of pseudoplastic fluids have focused on laminar jets (Gutfinger and Shinnar, 1964: Serth, 1972; Mitwally, 1978; Kumar et al., 1984; and Jordan et al., 1992). In most of these studies the authors attempt to develop similarity solutions for the laminar flow region. Douillard provides an excellent overview of work performed on submerged laminar non-Newtonian jets (1995). Since the mode of operation of the jets in the DSTs would have to be turbulent to be effective, we will assume that laminar jets will not be of concern in this problem.

Studies of turbulent non-Newtonian jets are limited to drag reducing polymers. A summary of some of the work in this area is given in McComb (1990). Barker (1973) performed measurements in jets consisting of dilute polymer suspensions and reported no effect on the mean velocity or turbulent intensity. In a study on a yield pseudoplastic jet, using a quantitative flow visualization technique, Shekarriz et al. (1995a) observed a macroscopic jet

behavior that was quite different from its Newtonian counterpart. They noticed that when the behavior index of a "power-law" fluid is sufficiently low, or if the fluid has true yield stress, the jet experiences a very rapid decay at a distance downstream which is directly a function of the nozzle exit velocity (an example of some of the results is provided in Figure 2.7).[11] They speculated that the shear rate in the jet reduces to the point that the fluid becomes extremely viscous and hence the jet undergoes a transition from inertially-dominated to viscous-dominated flow. Beyond the transition point the jet rapidly decays. This phenomenon has been compared to laminarization processes that often occur when mixing fluids that tend to become more viscous as a result of reactions in the processes. Hence, it was suggested that relaminarizing as a result of an increasing viscosity in the streamwise direction could be one reason for such rapid transition. However, since they observed the same global phenomenon in fully laminar jets of this fluid, Shekarriz et al. (1995a) concluded that the rapid decay transition was not caused by relaminarization of a turbulent jet, but might have been caused by the presence of a yield stress.

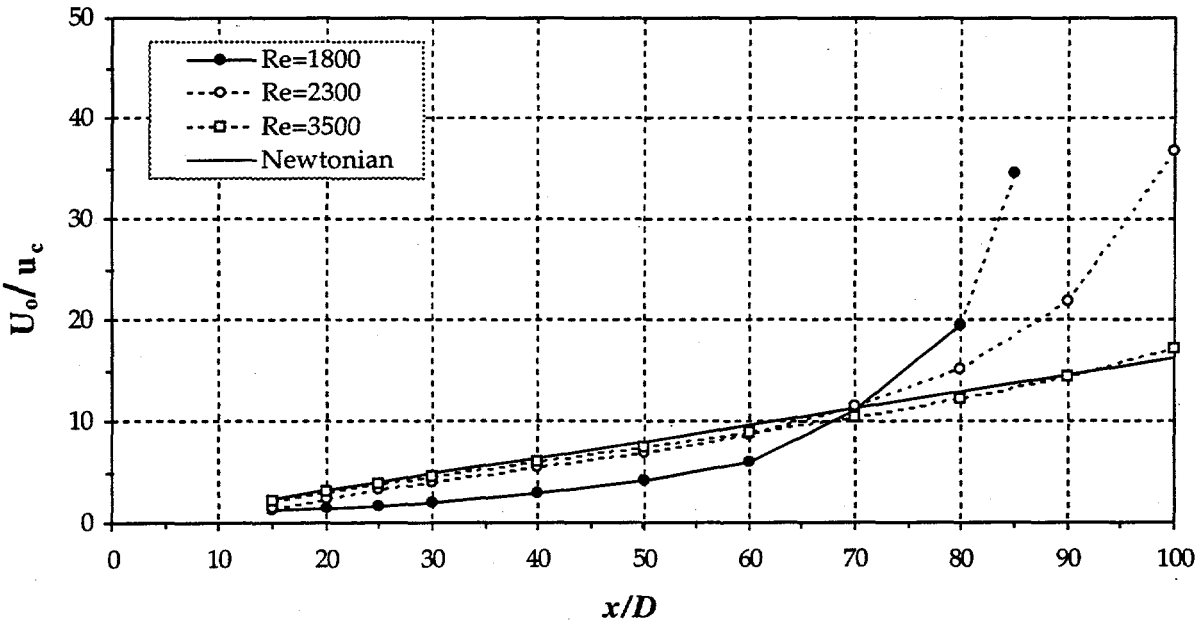

Figure 2.7. Decay Rate in Non-Newtonian Jets (Shekarriz et al. 1995b).

[11] If a power-law model is used, the behavior (or power-law) index becomes fairly small. However, if a yield pseudoplastic model such as Herschel-Bulkley is used, the behavior index becomes larger, but a finite yield is found in the model. Further characterization of this type of fluid (Carbopol solution) at these concentrations have found that the fluid had a true yield stress of ~1 Pa.

Douillard (1995) and Shekariz et al. (1995b) carried out further experiments to illucidate the primary reason for such rapid decay in the velocity. Using a laser Doppler velocimetry approach, they measured the velocity field and turbulence in a jet within a relatively large tank. When testing different rheologies of fluid, they found that indeed the centerline velocity decay became more severe as the fluid became more pseudoplastic. By measuring the velocity profiles across the jet at several streamwise locations, they were able to find the streamwise momentum and mass flux in the jet. Figure 2.8 shows the axial distributions of the momentum flux and mass flux in the jet. The non-Newtonian jet in this case had a yield stress of approximately 2.5 *Pa*.

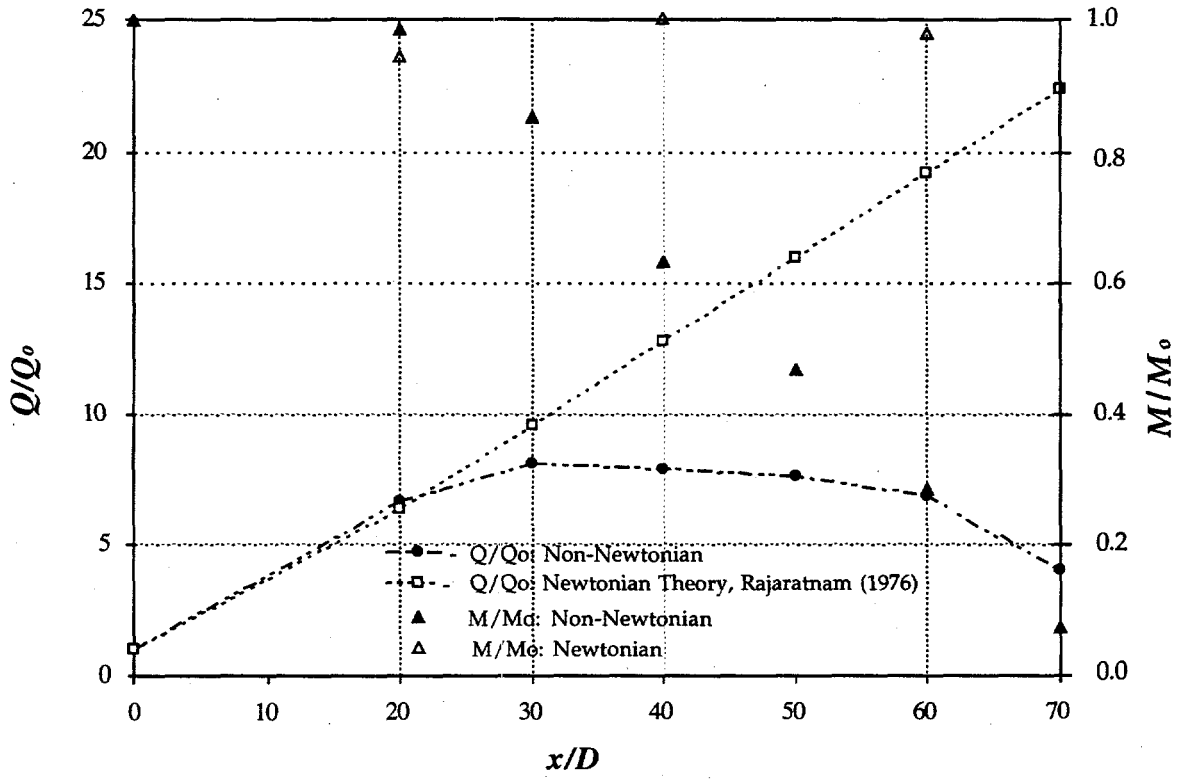

Figure 2.8. Axial Distributions of Mass and Momentum Flux in a Non-Newtonian (Yield-Pseudoplastic) Jet.

Since there may be several effects counteracting each other in the jet, we will look at the effect which we consider as the most dominant one in a fluid with yield stress. We have already discussed some of the detail in a separate report (Powell et al. 1997). However, we

will cover the summary and the crux of the analysis here for completeness. If we consider a jet that is submerged in a like fluid that has a yield stress,[12] then the momentum equation in an integral form for the jet appears as follows:

$$\frac{1}{2\pi}\frac{d}{dx}\left(\int_0^\infty 2\pi r\, dr\, \rho u^2\right) = -(r\tau)\Big|_0^\infty \tag{2.19}$$

where the fluid properties are as defined before and the geometry of the jet is similar to what is shown in Figure 2.1. Let's assume that the fluid follows a constitutive model defined by the Herschel-Bulkeley equation:

$$\tau = \tau_o + K\left(\frac{\partial u}{\partial r}\right)^n \tag{2.20}$$

where K and n are the materials properties referred to as the consistency factor and behavior index. τ_o is as before the materials yield stress. Substitution of Equation (2.20) into (2.19), integration from r=0 to $r\to\infty$, and using an appropriate model for the half-width of the jet as a function of the streamwise position yields the following relationship for the momentum flux in a non-Newtonian jet (see Appendix A in Powell et al. 1997 for the details and assumptions):

$$M^* \equiv \frac{M}{M_o} = 1 - 0.1\, x^{*2}(\tau_o/\rho u_o^2). \tag{2.21}$$

M is the axial momentum flux in the jet, superscript $x^*=x/D$, and subscript o denotes the conditions at the nozzle exit (x=0). The above equation is in fact consistent with our expectation that when a jet becomes Newtonian (with zero yield), then momentum flux in the jet becomes independent of the axial direction and remains equal to the initial mometum in the jet.

A similar approach may be adopted in deriving the equations representing the mass flux in the jet. In general, the mass flux and momentum flux are related through the following

---

12 In reality, we may observe similar behavior for fluids that are highly shear-thinning to the point that at very low shear rates it may have an apparent yield point. But from a theoretical point of view, we will consider this behavior as yield stress.

equation:

$$\frac{M^*}{Q^*} = \frac{\int_0^\infty r^*\, dr^*\, u^{*2}}{\int_0^\infty r^*\, dr^*\, u^*} \approx \overline{u^*} \tag{2.22}$$

where Q is the axial mass flux in the jet, $Q^* = Q/Q_o$, $r^* = r/D$, $u^* = u/U_o$, and the overbar refers to the average axial velocity at each axial position of the jet. The average axial velocity is closely approximated to be half of the centerline velocity at each axial location. Assuming a linear variation in the centerline velocity, we find that the average velocity varies inversely as x.

$$\overline{u^*} \cong C/x^* \,. \tag{2.23}$$

The proportionality constant C for a Newtonian fluid turns out to be ~3.15. Substituting Equation (2.23) into (2.22) and in turn substituting the resultin relation into Equation (2.21) will yield the following relation for the mass flux:

$$Q^* = 0.32\, x^* \left[1 - 0.1\, x^{*2} (\tau_o / \rho u_o^2) \right]. \tag{2.24}$$

Rajaratnam (1976) shows that for a Newtonian jet, Q^* increases as $0.32\, x^*$ which is consistent with Equation (2.24) for the asymptotic limit at which the yield stress vanishes. Figure (2.9) is a plot of both the momentum flux and mass flux as a function of x^* for a fluid with a yield stress on the order of 10 *Pa*, a density of 10^3 *Pa*, and an initial jet velocity of 10 *m/s*.

When we compare the results shown on Figure 2.10, which were obtained from the models develped in this section, to the experimental data that was presented for a yield pseudoplastic jet, we see that at the minimum a very good qualitative agreement exists between them. The trend in the quantitative information also suggests that the models for M^* and Q^* may not be too far off. We know that at the asymptotic limits, the predictions are accurate. Figure 2.9 also suggests that in the near-field of the jet, say for $x^* < 30$, the jet does not deviate too far from the Newtonian behavior. We will discuss some of these results further in Section 4.0 and in the future reports.

In summary, based on the experimental observations and comparison to a simple model for non-Newtonian jets, it is fair to say that for yield fluids, the momentum flux within the jet drops as x^{*2}. The resulting mass flux in the jet tends to go through a maximum and drops to zero as rapidly as the momentum flux in the downstream direction.

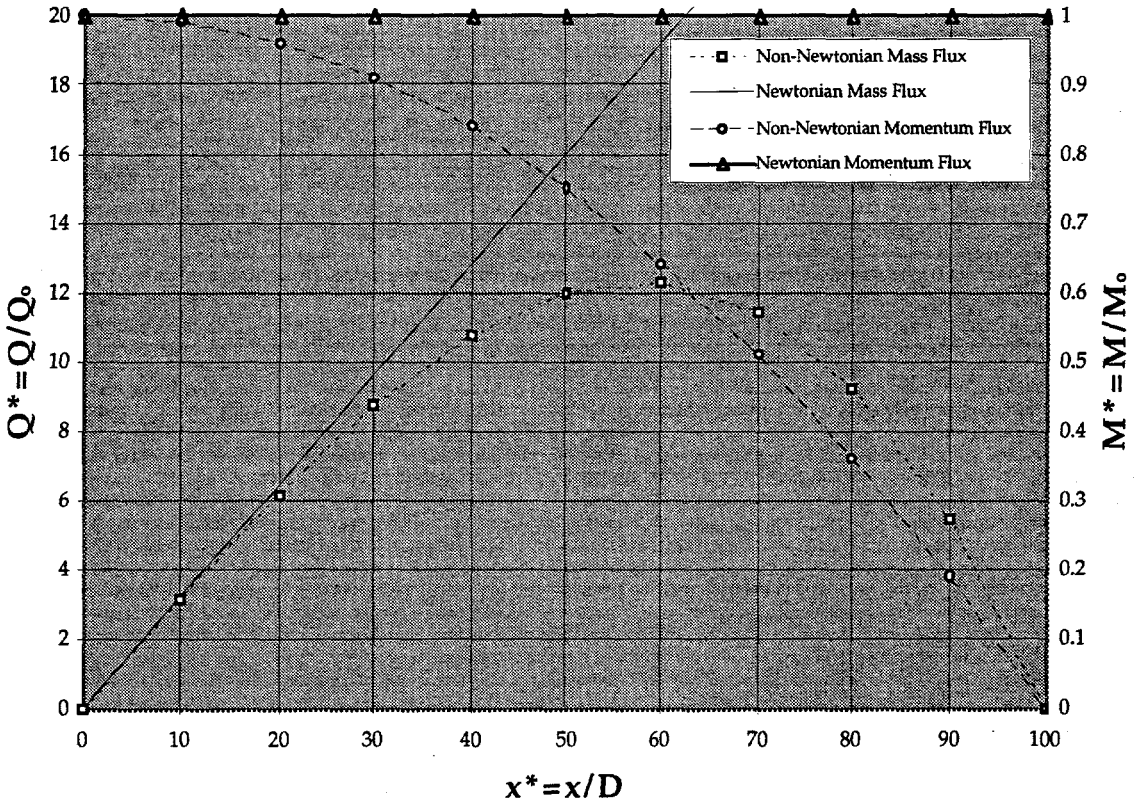

Figure 2.9. Mass and Momentum Flux in Newtonian and Non-Newtonian Yield Stress Jets.

3.0 Scaled Experiments: 1/50 Scale

In several previous studies at PNNL correlations were developed between sludge simulant properties and the ECR (see Powell et al. 1997). A scaleup methodology was developed for performing scaled sludge mobilization tests nearly two decades ago (Horowitz 1980), but the validation of this methodology has been the subject of several studies some of which have not been published.

The experiments described in this section were conducted in an effort to evaluate sludge mobilization test scaling. Two aspects of sludge mobilization scale up are of interest. First, the scaling methodology predicts linear ECR scaling. That is, assuming identical sludge properties and nozzle exit velocities, full-scale ECRs will be twenty-five times larger than the 1/25-scale ECRs. Similarly, ECRs measured in a 1/50-scale test will be half the size of the 1/25-scale ECRs. Thus, the ECR normalized by the diameter of the tank in each scale should be a constant and the same for all scales.

The second aspect of ECR scaling is the scale up of ECR growth rate data. According to the scale-up methodology, the normalized ECRs (ECR divided by a consistent measure of the test length-scale, such as the tank diameter) will grow at proportionally faster rates at smaller scale. That is, the time required to reach any given normalized ECR will be twenty-five times longer at full-scale than is observed at 1/25-scale. This approach of scaling, of course, presumes that the appropriate property of the slurry in the full-scale conditions is utilized, as discussed in the previous sections.

Both these aspects are important from the perspective of the designers and operators of the full-scale double-shell tank retrieval systems at Hanford. The fraction of sludge that will be mobilized by a given mixer pump system design is predicted based on the correlations developed through scaled testing *and* based on the assumed linear scaling of the ECR. Establishing a more robust predictive ability based on purely empirical correlations is the motivation for evaluating the ECR scaleup procedure.

ECR growth rate scale up will be one of the means of estimating how long the mixer pumps must be operated at full power to reach the final ECR (i.e., the point where no further

ECR growth occurs because of the ability of the sludge to resist the mixer pump jets). If linear scaling of the ECR growth rate is deemed applicable, then the 1/25-scale ECR vs. time data can be used to establish a range of predicted mixer pump operation times. The range predicted by the 1/25-scale data is found to be large (between 1 day and > 30 days at full-scale) due to the variance in the properties of the mixtures used.

In this section, we will describe the sludge mobilization tests that were conducted in a 1/50-scale (approximately) tank. More than fifty 1/25-scale sludge mobilization tests were conducted between fiscal years 1993 and 1995. So in the current study we decided that the 1/50-scale tests would be configured to represent a 1/2-scale test of a specific 1/25-scale test, which was selected to be Test 1-K from the fiscal year 1994 test series (Powell et al. 1995).

Testing at a scale larger than 1/25-scale is preferable because the physical phenomena that control mobilization may change with scale, so larger-scale tests are likely to more closely approximate the sludge mobilization process in a full-scale tank. However, the cost of conducting tests at a larger scale (1/12-scale, for example) were deemed prohibitive. Thus, testing at a scale smaller than 1/25-scale for the comparison was done. Indeed, once scaling laws are appropriately utilized, then it should make, in principle, no difference at what scales the experiments are performed.

3.1 Experimental Setup and Procedure

The 1/50-scale testing was conducted in a 49 *cm* (1.6 *ft*) diameter Plexiglas™ tank. Before testing, the bottom of the tank was marked with concentric circles spaced at 2 *cm* intervals. Eight radial lines (spaced at 45° intervals) were drawn from the tank center to the tank wall. During testing, the location of the sludge interface (viewed from beneath the clear-bottomed Plexiglas tank) was measured along each of these eight lines, using the concentric circles to determine the radial distance between the tank center and the interface. The ECR is the average of the eight readings.

A single, simulated mixer pump was positioned in the center of the tank for each test. The slurry enters the suction of the simulated mixer pump and travels up through a flexible hose to the intake of a centrifugal pump. The slurry flow rate is monitored with a calibrated magnetic flow meter and manually controlled by a ball valve. The pressurized slurry flows down through the mixer pump and out the horizontal, diametrically opposed nozzles (see Figure 3.1).

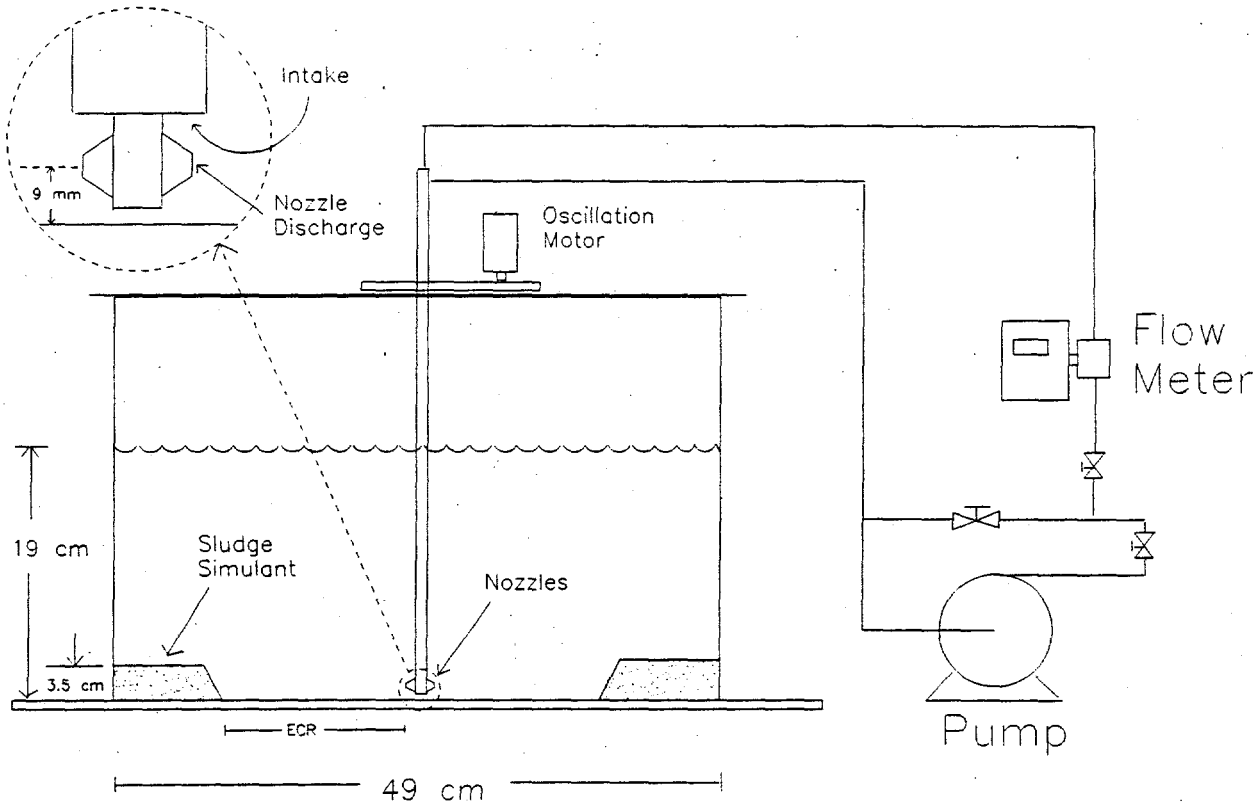

Figure 3.1. Schematic of 1/50-Scale Test Facility

The mixer pump nozzles were located such that their centerline distance above the tank floor was 1/50th of the planned full-scale distance of 46 *cm* (18 *in*). The nozzles were machined from stainless steel. For most tests, 0.3 *cm* diameter nozzles were used although 0.6-*cm* nozzles were used in some tests. The nozzles were designed such that the nozzle exit velocity profile would be reasonably uniform. Figure 3.2 is a sketch of the 0.6 *cm* nozzle used for Tests 50K-7, 50K-8, and 50K-11. The 0.3 *cm* nozzle was designed to have a similar entrance region and straight section.

Eleven 1/50-scale tests were conducted as generally described below. A mass corresponding to approximately 6.6 *L* (1.7 *gal*) of sludge simulant was placed into the 1/50-scale tank and smoothed to a ~ 3.5 *cm* (1.4 *in*) uniform thickness. The 1/50-scale mixer pump assembly was then positioned in the tank such that the mixer pump centerline coincided with the tank centerline. Twenty-five liters of simulated supernatant liquid (water) was then pumped into the tank. The resulting liquid surface was approximately 19 *cm* (7.5 *in*) above the tank bottom. Care was taken to avoid disturbing the sludge bed while adding the liquid.

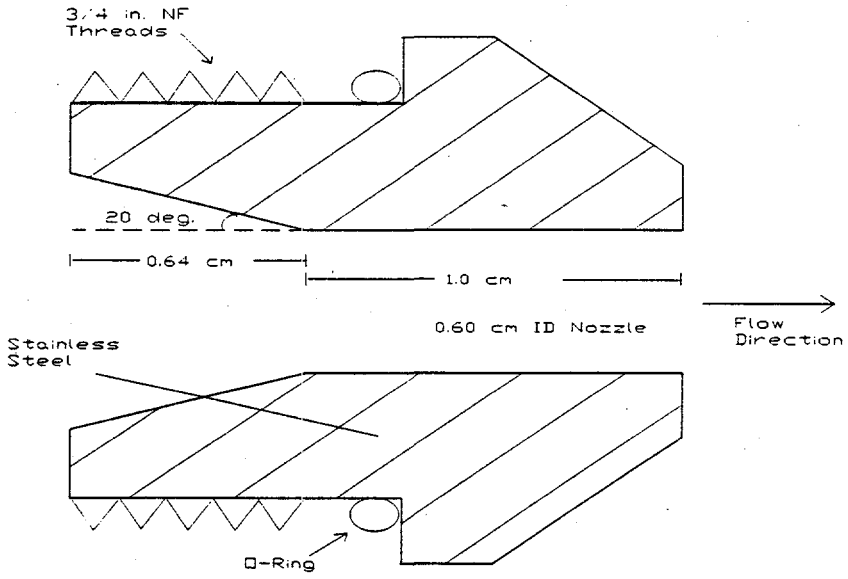

Figure 3.2. Sketch of 0.6 *cm* Nozzle Cross-Section

The mixer pump assembly was continuously oscillated through 180° of rotation during the tests at a rate equivalent to 7 rpm, which is twice the rotation rate used for the 1/25-scale sludge mobilization test to which the data were compared. Linear scaling of the pump column rotation rate is consistent with the scaling methodology described earlier in this report.

To begin each test, the centrifugal pumps were turned on and the flow control valve opened to obtain the desired flow rate, which was scaled based on the flow rate used in 1/25-scale Test 1-K. Frequent measurements were made of the distance between the tank centerline and the sludge bank (defined as the effective cleaning radius) along each of the 8 radial lines scribed in the bottom of the tank.

Effective cleaning radius (ECR) measurement continued until the average of the eight ECRs was observed to either stabilize (zero growth rate) or otherwise reach the tank wall. At that point, the slurry was pumped out of the tank to expose any remaining sludge bank.

Four different types of slurry pumps were used. Tests 50K-1 and 50K-2 used a 2 *hp* centrifugal pump. Tests 50K-3 and 50K-4 used a small 1/8 *hp* gear pump, Test 50K-5 used a 1/3 *hp* sump pump, and tests 50K-6 through 50K-11 used a 1/2 *hp* centrifugal (TEEL) pump. The switch to a smaller pump was made after Test 50K-2 in an effort to avoid the rapid increase in slurry temperature that resulted when the 2-HP pump was used. The 1/8 *hp* gear pump solved the temperature increase problem, but it was not sufficiently reliable. It failed

during Test 50K-4. The 1/3 *hp* sump pump used in Test 50K-5 also failed prematurely. A 1/2-*hp* pump, which resulted in an acceptable rate of temperature rise, was then obtained and used for the remaining tests.

In parallel with each test, samples of the sludge simulant were characterized. Measurements were made of the sludge shear strength (τ_s) and weight percent solids to ensure that it was consistent with the 1/25-scale sludge properties. The shear strength was measured using a four-bladed shear vane. The peak torque required for slow rotation of the vane submerged in the sludge simulant is used to estimate shear strength. This shear strength measurement technique is commonly used in soil mechanics and is described in Powell et al. (1995).

The tank waste sludge was simulated using EPK Pulverized kaolin clay from Feldspar Corporation (Edgar, Florida). The clay was mixed to a nominal concentration of 65 wt% solids using an electric mixer and placed inside the tank. This concentration and clay type was identical to that used in 1/25-scale Test 1-K, to which all of the 1/50-scale results are compared.

Test 1-K was selected as the 1/25-scale test for comparison to all the 1/50-scale tests for three reasons. First, the sludge simulant was kaolin clay, which has been found to exhibit comparatively little dependence of the ECR on sludge properties (Powell et al. 1995). Thus, small variations in the simulant strength would not be expected to significantly affect the ECR measurements. Second, more than a dozen 1/25-scale tests were conducted using kaolin/water sludge simulants, so the ECR growth rate for kaolin/water and its dependence on sludge strength is relatively well understood. Third, Test 1-K was conducted using a single mixer pump flow rate rather than multiple flow rates as was done for many 1/25-scale tests and Test 1-K was continued until ECR growth stopped. The ECR/U_oD vs. time data from Powell et al. (1995) for Test 1-K are given in Figure 3.3.

The kaolin/water sludge simulant used in Test 1-K had a shear strength measured at 2.1± 0.1 *kPa* and a U_oD of 498 ± 7 cm^2/s (D was 0.6 *cm*). The 1/50-scale tests were generally conducted using a 0.3 *cm* diameter nozzle with a U_oD of 249 ± 10 cm^2/s (exceptions are noted where appropriate). The sludge simulants used in 1/50-scale testing were prepared to have the same composition as the Test 1-K simulant. The 1/50-scale simulant shear strengths and wt%

solids were measured and found to be nearly identical to that of Test 1-K. Shear strengths for the 1/50-scale tests ranged from 1.9 ± 0.3 *kPa* to 2.4±0.3 *kPa*. Solids concentrations (weight loss on drying to 210 ℃) for the 1/50-scale sludge simulants ranged from 63.0 ± 0.3% to 64.3 ± 0.3%. The Test 1-K solids concentration was 64.2 ± 0.2%.

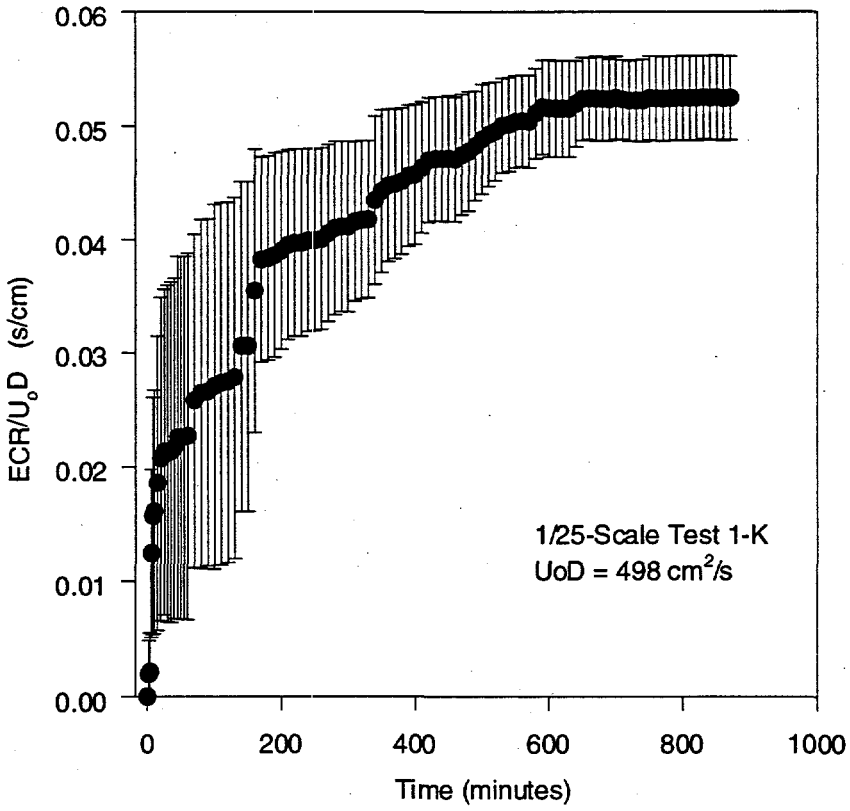

Figure 3.3. 1/25-Scale Test 1-K ECR Growth Data.

3.2 Results

The results of all eleven 1/50-scale tests are summarized in the table below. Several tests yielded no useful ECR data because of experimental difficulties. Tests 50K-4 and 50K-5, for example, were stopped prematurely because the slurry pump failed. Similarly, lifting of the sludge bank early in Test 50K-6 resulted in very rapid mobilization of all the sludge. Sludge bank lifting is unlikely to occur in a full-scale operation (see Powell et al. 1995) and did not occur in 1/25-scale Test 1-K, so the data for these tests were not used in the scale-up comparison.

Table 3.1. 1/50-Scale Sludge Mobilization Test Results

Test No.	Test Parameters	Results	τ_s *kPa*	Sludge wt%
50K-1	$U_oD = 249 \pm 10\ cm^2/s$ $D = 0.30\ cm$, 2*hp* pump nozzles 5 mm too high	ECR grew to tank wall in 150 minutes. Slurry temp. increased rapidly.	2.4 ± 0.3	64.1
50K-2	$U_oD = 249 \pm 10\ cm^2/s$ D= 0.30 *cm*, 2*hp* pump nozzles set to scaled height	ECR grew to tank wall in 170 minutes. Slurry temp. increased rapidly.	2.1 ± 0.2	63.5
50K-3	$U_oD = 140 \pm 10\ cm^2/s$ for 280 *min.* then set to 249 cm^2/s until 720 *min.*. D= 0.30 *cm*, 1/8*hp* pump	ECR grew to 13.6 ± 2.9 *cm* by 280 *min.* then to 18.2 ± 2.8 *cm*. Insignificant temp. increase	2.0 ± 0.3	63.3
50K-4	$U_oD = 249 \pm 10\ cm^2/s$ $D = 0.30\ cm$, 1/8 *hp* pump	slurry pump failed	2.3 ± 0.2	63.8
50K-5	$U_oD = 249 \pm 10\ cm^2/s$ D= 0.30 *cm*, 1/3 *hp* pump	slurry pump failed	2.0 ± 0.2	63.5
50K-6	$U_oD = 249 \pm 10\ cm^2/s$ $D = 0.30\ cm$, 1/3 *hp* pump	ECR reached tank wall in about one hour. Sludge bank lifting problems early in the test.	1.9 ± 0.3	63
50K-7	$U_oD = 249 \pm 10\ cm^2/s$ $D = 0.60\ cm$, 1/2 *hp* pump	ECRs along 2 lines reached wall in 30 minutes because of sludge lifting. Remainder of tank reached 18.3 ± 1.4 *cm* by 390 min.	2.1 ± 0.3	63.2

Test No.	Test Parameters	Results	τ_s *kPa*	Sludge wt%
50K-8	$U_oD = 249 \pm 10\ cm^2/s$ $D = 0.60\ cm$, 1/3 *hp* pump	ECRs along 3 lines reached wall in about 1 hour because of sludge lifting. Remainder of tank reached 18.6 ± 2.3 cm by 410 min.	2.3 ± 0.2	64
50K-9	$U_oD = 249 \pm 10\ cm^2/s$ $D = 0.30\ cm$, 1/3 *hp* pump wire mesh secured to bottom of tank in regions between ECR lines	Some sludge lifting evident along ECR lines. ECR reached 20.2 ± 1.7 *cm* by 240 minutes.	2.3 ± 0.2	63.9
50K-10	$U_oD = 249 \pm 10\ cm^2/s$ $D = 0.30\ cm$, 1/3 *hp* pump wire mesh secured to entire bottom of tank	ECR reached tank wall (ECR = 22 *cm*) along all lines at 180 *min.*	2.3 ± 0.3	64.3
50K-11	$U_oD = 249 \pm 10\ cm^2/s$ $D = 0.60\ cm$, 1/3 *hp* pump wire mesh secured to entire bottom of tank	ECR reached tank wall along 7 of the 8 ECR lines by 220 minutes. Final line reached wall at 300 minutes.	2.2±0.2	64.4
1-K	$U_oD = 498 \pm 7\ cm^2/s$ $D = 0.60\ cm$, 2 *hp* pump	ECR grew to 25 ± 2.2 *cm* in 600 minutes and then stopped.	2.3 ± 0.3	64.3

The data in Table 3.1 imply that the ECRs observed at 1/50-scale for both the 0.3- and 0.6-cm diameter nozzles are significantly larger than was expected based on the previous 1/25-scale test results. Further, the 1/50-scale ECRs grew more quickly than predicted. Linear scaling of the Test 1-K mobilization rate data implies that roughly 600/2 = 300 minutes should be required to reach the final ECR. Instead, less than half that much time was required. Possible explanations for the observed deviation from a linear scaling behavior are discussed below.

3.2.1 ECR Scaling

ECR/U_oD vs. time data for 1/50-Scale tests 50K-1, 50K-2, 50K-9, and 50K-10 are plotted along with the scaled data from 1/25-scale Test 1-K in Figure 3.4. The 1-K data were scaled by dividing all the time values by 2.0. The four 1/50-scale tests identified on the plot were selected because relatively few problems with sludge bank lifting were observed during these tests, and all four tests were conducted using the same operational parameters (i.e., U_oD

= 249 cm^2/s, D = 0.3 cm).

Clearly, the observed ratio ECR/UoD for all 1/50-scale tests are significantly larger than what is predicted by the 1/25-scale data. This result suggests that if tests at 1/50-scale over-predict the 1/25-scale ECRs, then perhaps the 1/25-scale correlations over-predict the full-scale ECRs. Several possible explanations for this unexpected result may be possible. The most obvious explanation might be that the ECR really does not scale linearly as had been assumed. Before such a conclusion can be reached, however, it is necessary to determine whether any other factors might be responsible for the unexpected results.

It might be suggested that 1/25-scale Test 1-K was somehow atypical. If so, then maybe more tests at 1/25-scale would show that larger ECRs are obtained which are consistent with linear ECR scaling of the 1/50-scale results. This is not the case. As was mentioned earlier, kaolin clay sludge simulant was selected because it has been used for many 1/25-scale mobilization tests and has been found to give consistent results. A total of 15 separate 1/25-scale tests have been conducted using various mixtures of kaolin clay and water to simulate the sludge. Despite testing over a range of shear strengths, from less than 0.3 *kPa* to more than 4.0 *kPa*, the final ECR/U_oD's obtained for the 1/25-scale tests were always in the range of 0.045 to 0.062 *s/cm*. Four tests with sludge shear strength in the 1.5 to 2.5 *kPa* range have been conducted and these tests yielded ECR/U_oD's between 0.052 and 0.06 *s/cm*. It seems, therefore, unlikely that so many 1/25-scale tests could all be "atypical." Thus, this explanation does not seem to provide an appropriate interpretation of the data.

The 1/25-scale tests using kaolin clay sludge simulants agree reasonably well with the ECRs observed during full-scale testing of mixer pumps using kaolin clay at the Savannah River Site (see Powell et al. 1997). The full-scale tests produced an average ECR/U_oD of 0.064 ± 0.006 *s/cm*, which is in good agreement with the range of 1/25-scale results reported earlier. The Savannah River kaolin clay simulant was not characterized well enough for a definitive comparison, but it is encouraging that the results are consistent with the 1/25-scale data. It would be surprising if the 1/25-scale results scale up to the full-scale tests performed at SRS but do not scale down to the current 1/50-scale.

Another possible explanation for the 1/50-scale data is that there is a qualitative difference in the mechanisms of sludge mobilization between 1/50-scale and 1/25-scale. This is not as unreasonable as it might first sound. Lifting of the sludge bank during many of the

1/50-scale tests was a problem, but no sludge bank lifting was observed during the testing of kaolin sludge simulants at 1/25-scale. Sludge bank lifting becomes progressively less likely as the scale of the test is increased because the pressure available for lifting the sludge bank (from the impinging fluid jets) remains the same for all the scales, based on a Newtonian model, while the hydrostatic pressure at the bottom of the sludge layer, which resists the lifting pressure, increases linearly with the scale. However, we believe that for the four 1/50-scale tests outlined above, the sludge bank lifting was negligible and therefore its effect on ECR can be ignored.

Efforts were made to eliminate the potential for sludge bank lifting during the 1/50-scale tests. Tests 50K-9 through 50K-11 were conducted with a fine wire mesh glued to the tank floor to improve the adhesion of the sludge to the tank. No significant differences were noted between the tests where the screen was used and those tests where the screen was not used but bank lifting was not evident (i.e., 50K-1 and 50K-2). This implies that it is unlikely that sludge bank lifting is the culprit.

Another possibility is that there is a difference in the decay rates of the 1/25-scale and 1/50-scale mixer pump jets. The same scaled mixer pump assembly was used for both scales of tests. Smaller nozzles (0.3 *cm* instead of 0.6 *cm*) were used for most of the 1/50-scale tests. The total slurry flow rate through the 1/25-scale nozzles is, therefore, twice that of the 1/50-scale nozzles when equal U_o's are used (thereby giving a linearly scaled U_oD). Just before entering the mixer pump nozzles, the slurry flows down through the mixer pump column and makes a sharp 90-degree turn. This tortuous flow path has previously been observed to induce swirl in the fluid jets when larger (0.9 *cm* diameter) nozzles are used in the mixer pump assembly (Powell et al. 1995). Because the 1/25-scale tests require twice the slurry flow and larger-diameter nozzles, they are more susceptible to the swirl problem than are the 1/50-scale tests. Swirl causes fluid jets to lose their momentum more rapidly. If significant swirl was induced in the 1/25-scale jets, all of the 1/25-scale ECRs would tend to be biased low.

To evaluate this possibility, tests 50K-7, 50K-8, and 50K-11 were performed using a nozzle diameter of 0.6 *cm*, which is the same as was used in the 1/25-scale tests. The test results are shown in Figure 3.5. There appears to be a difference in both the final ECR and the ECR growth rate between the tests using the 0.3 *cm* nozzles and those using the 0.6 *cm* nozzles. The data for tests 50K-7 and 50K-8 have relatively large error bars because in each of these tests a portion of the sludge bank was lifted by the jets early in the test and this resulted in rapid and complete mobilization in those portions of the tank. Thus, the average ECRs shown

for these two tests are actually larger than shown in the figure. If the portions of the tank where sludge lifting occurred are ignored, the resulting average, final ECR/U_oD for tests 50K-7 and 50K-8 are 0.073 ± 0.006 and 0.075 ± 0.009 *s/cm*, respectively. Both values are somewhat smaller than the 0.090 *s/cm* observed for most of the 0.3 *cm* nozzle tests.

Fluid jet swirl is also judged to be an unlikely explanation, however. The jet swirl problem in the 1/25-scale mixer pump apparatus was studied previously (Powell et al. 1995) and found to be relatively unimportant when nozzles equal to or smaller than 0.6 *cm* were used. This was demonstrated by installing flow-straightening vanes upstream of several different nozzle sizes. With the flow straighteners installed, the ECRs produced by 0.4 *cm*, 0.6 *cm*, 0.75-*cm*, and 0.9 *cm* diameter nozzles (all at equal U_oD's) were all equivalent. Further the performance of the 0.6 *cm* nozzles *without* the flow straighteners was not significantly different than that of the 0.6 *cm* diameter nozzles with the flow straighteners.

Whether differences in the jet decay rates can explain the differences between the 1/25-scale and 1/50-scale ECRs could potentially be resolved by measuring the velocity profiles via an anemometry approach. This technique would likely detect any unexpected differences the decay rates of the average jet velocities, but might not detect differences in turbulence levels, which might also affect the rate and extent of sludge mobilization (see Section 4.0 regarding jet turbulence).

3.2.2 ECR Growth Rate Scaling

Figure 3.4 is the time history plot of the ECR for the 1/50 scale tests. Note that most of the data fall within the predicted uncertainty band. Figure 3.4 shows that the 1/50-scale ECRs grow more quickly and to larger distances than is predicted based on 1/25-scale Test 1-K. If the expected linear scaling of the mobilization rate occurred, tests at 1/50-scale would require about half as much time to reach the final ECR as tests at 1/25-scale. The Test 1-K data shown in Figure 3.4 have been modified by taking the original data and compressing time by a factor of two. Thus, if linear scaling of mobilization time occurred, the 1/50-scale data should fall within experimental uncertainty of the Test 1-K values plotted in Figure 3.4.

It appears that the 1/50-scale ECRs grow roughly twice as fast as expected. This is four times faster than 1/25-scale rather than the expected two times. However, the 1/50-scale ECR data shown in Figure 3.4 do not provide a good estimate for the required mobilization time

(i.e., the mixer pump operation time required to effectively reach the final, asymptotic ECR) because all of the sludge was mobilized in these tests.

Test 50K-3, however, was run using a lower U_oD to ensure that some sludge would remain unmobilized and the time required to reach the final ECR could be measured. The data for Test 50K-3 are shown along with the Test 1-K data in Figure 3.5. Roughly 280 minutes is required for the Test 50K-3 ECR to stop growing. This is consistent with the prediction of 300 minutes made based on Test 1-K. The Test 50K-3 data, therefore, supports linear scaling of mobilization time. More testing would be required to provide assurance that mobilization time actually does scale linearly, but resolution of the linear ECR scaling issue is judged to be a higher priority.

Regardless of whether mobilization time scales linearly as implied by Test 50K-3, the range of mobilization times observed in 1/25-scale testing is too broad for useful predictions to be made. The best guidance available for predicting the required mobilization time in the Hanford double-shell tanks is obtained from the full-scale mixer pump tests at the Savannah River Site where mobilization times in the range of 50 to more than 500 hours were measured (Hamm et al. 1989; Churnetski 1982).

In summary, we believe the 1/50-scale and 1/25-scale tests performed to date are statistically significant enough to consider as reliable sources of data. Although, in terms of linear scaling, they do not seem to collapse onto a single set of curves. Potentially, by including one of the mechanisms described in the previous section, and by including the results of the 1/12-scale tests, one will be able to conclusively provide an empirical correlation which can be effectively used. To properly use such a correlation, one presumes that the appropriate properties are used for the prediction of full-scale mobilization conditions. This requirement holds irrespective of what predictive tools are being utilized.

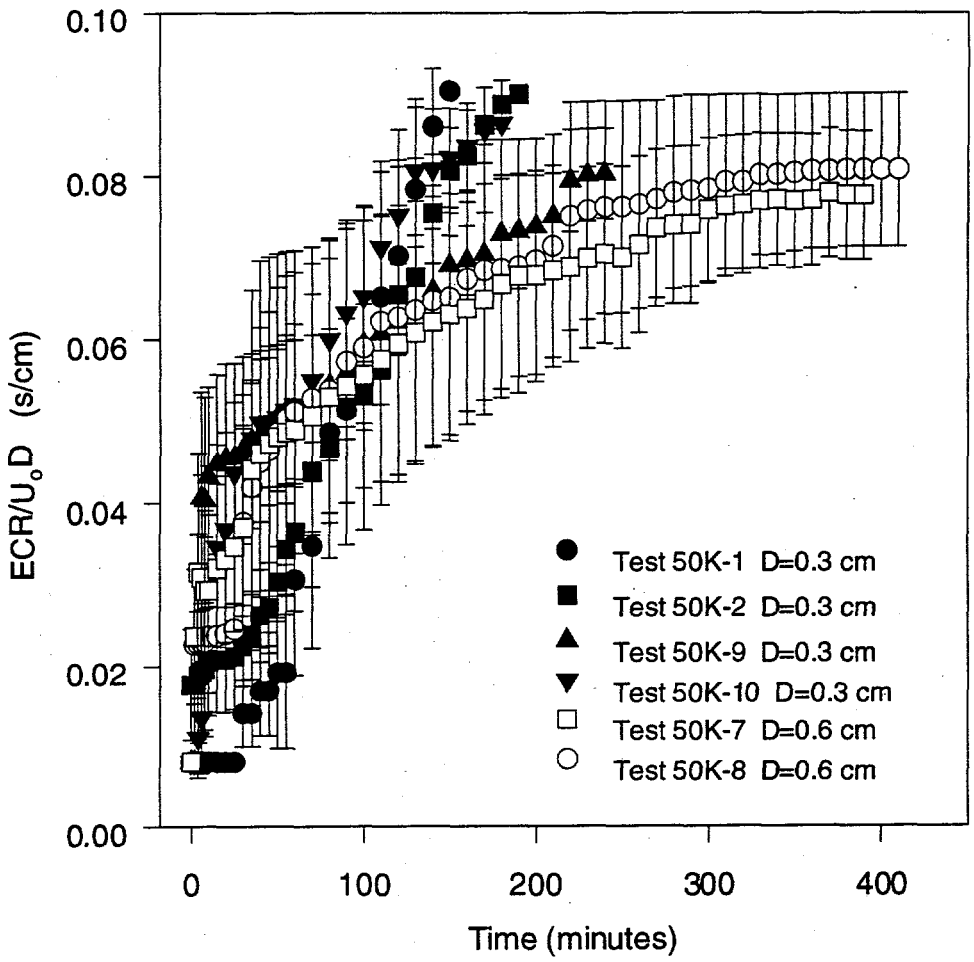

Figure 3.4. 1/50-Scale ECR Growth Rate Data for $D = 0.3\ cm$ and $D = 0.6\ cm$

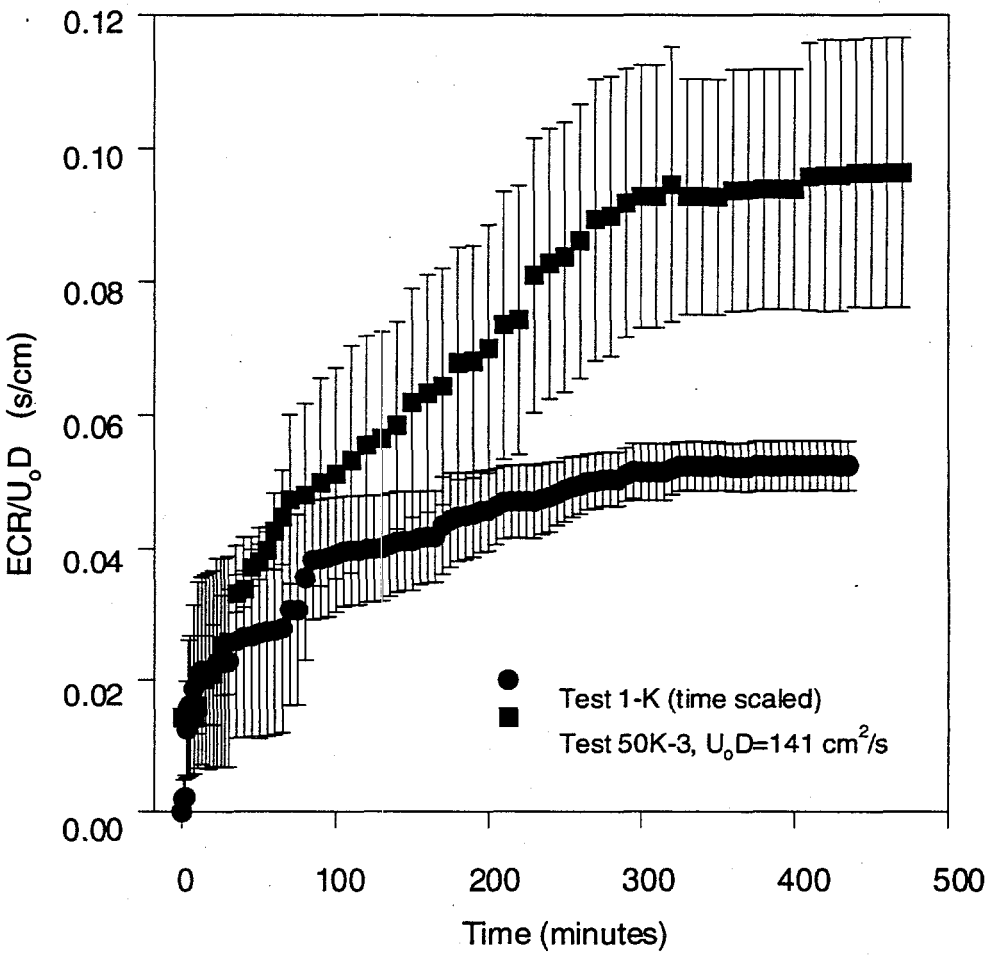

Figure 3.5. Mobilization Rate Data for Tests 50K-3 and 1-K

4.0 Homogeneous Fluid Jet Experiments

The main purpose of the homogeneous fluid jet experiments is to generate an accurate quantitative set of data to: 1) understand the physics of flow and mixing phenomena which will take place in the radioactive waste tanks at Hanford during the mobilization phase of retrieval, 2) develop scaling correlations that are valid at a wide range of scales, including the scales of double-shell tanks, and 3) validate the computational codes for predicting the different mixing conditions generated by the mixer pumps.

Consistent with our earlier discussion of the need for separate effects experiments, the approach adopted in the study described in this section is to identify the expected range of rheological characteristics of the waste. The jet hydrodynamics are then simulated in the laboratory with an appropriate set of mixtures. By using well-designed and carefully executed laboratory experiments utilizing accurate and reliable diagnostic techniques, we expect to provide new insight in the hydrodynamics of turbulent jets of various rheological characteristics.

Recall that in Section 2.4 we developed a model, based on turbulent kinetic energy budget or conservation, to see the functional dependence of the turbulent kinetic energy or turbulent intensity within the jet on the flow geometry and dynamics. We found, much to our surprise, that for a Newtonian jet the turbulent intensity was only a function of the flow geometry and not on the dynamics. Further, we are currently searching to find additional data, information, or theory that covers the same problem but with a non-Newtonian fluid. So our immediate goal during fiscal year 1997 was to perform some experiments that (1) verifies the validity of the (scaling) model developed in Section 2.4 for a Newtonian fluid and (2) repeats the same experiments for non-Newtonian fluids to see how the jet characteristics change. Within this section, we will provide the measurement background and principles, describe our experimental approach and tests performed, and finally present and discuss the results of these experiments.

4.1 Turbulence Measurement Principles

To accurately measure the jet turbulence, we resorted to the use of a popular technique called Laser Doppler velocimetry (LDV). LDV is an optical technique that allows the

measurement of the local, instantaneous velocity of tracer particles suspended in the flow, too small to interfere with the flow. The particular features of the LDV system which were suitable for our measurements are: 1) it is non-intrusive so it creates no flow disturbances, 2) velocity measurements are independent of the ambient conditions, 3) it has high accuracy with excellent spatial and temporal resolution, and 4) it has a wide dynamic range that extends from natural convection to very high velocities. The non-intrusive feature of the LDV technique is particularly useful in characterizing flows within an enclosure, where as utilizing invasive probes, such as hot wire and hot film anemometry, would result in disturbances to the recirculation patterns and turbulence.

The LDV setup utilized in this study is based on a dual-beam arrangement. The dual-beam arrangement consists of two crossing laser beams of identical wavelength (e.g. λ=514 *nm*), as shown in Figure 4.1. The cross-section of these beams forms an ellipsoidal intersection region referred to as the measurement volume. The dimensions of the probe volume (l_p and d_p) depend on the diameter of the incident laser beams (d_l) and their half angle of intersection ($\alpha/2$). The measurement volume dimensions typically vary between 30 to 1000 μm. Within the measurement volume parallel layers of bright and dark fringes are formed by the interferene of the two beams. The fringe spacing is linked to the wavelenght of the laser beam and the half angle between the two beams:

$$d_f = \frac{\lambda}{2 \sin(\alpha/2)}. \tag{4.1}$$

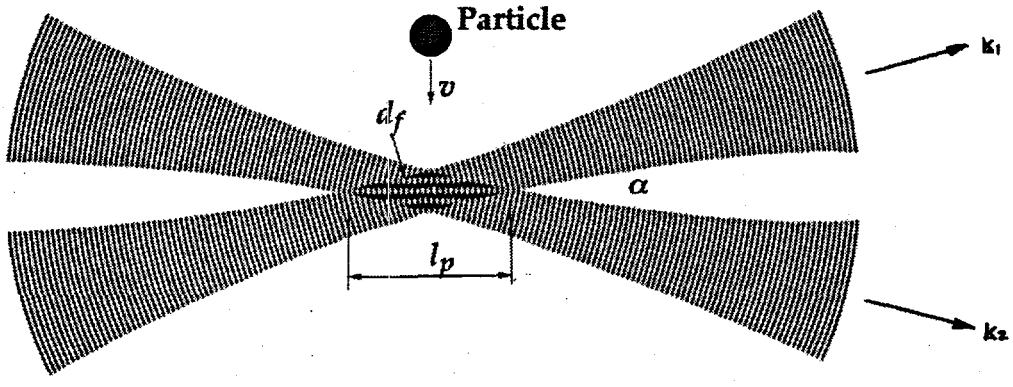

Figure 4.1. Dual-Beam LDV Measurement Volume Geometry

To measure the flow velocity, seed particles were added to the flow field as tracers. The particular seed particles used in this study were 14 μm diamter silver-coated hollow galss particles made by Potters Industries, Cleveland, Ohio. These particles were small and neutrally buoyant enough to follow the turbulence in the fow field as closely as possible and large enough to scatter a sufficient amount of light for higher signal-to-noise ratios.

As a tracer particle traveling with a velocity v crosses the measurement volume, it scatters pulsed light as it moves across the fringes. A trace of a sequence of pulses from particles moving across the measurement volume, Doppler bursts, is shown in Figure 4.2. The pulse frequency of the scattered light is linked to the Doppler frequency shift, f_D. The velocity v can be calculated from the Doppler frequency using the following relationship:

$$v = d_f \cdot f_D = \frac{\lambda \cdot f_D}{2 \sin(\alpha/2)}. \tag{4.2}$$

Velocity v is the component of particle velocity in the plane of the two incident beams and orthogonal to the bisector of the beams. Thus, in order to determine the velocity component v one needs to know only the wavelength of the incident light, the angle of intersection, and the Doppler shift frequency of the scattered light. Implicit in the above discussions is the requirement that the intersecting beams should be at a distinct wavelength. If two components of velocity are to be measured simultaneously then two distinct wavelengths can be used for each pair of intersecting beams (e.g. 488 *nm* and 514 *nm*).

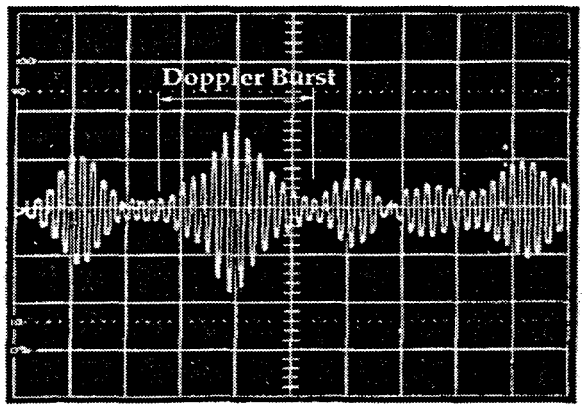

Figure 4.2. Doppler Bursts Sent by Particles Moving Across the LDV Measurement Volume

Since pure frequency measurement does not reveal the directionality of the velocity component other measures have to be introduced to resolve directional ambiguity on the velocity. Ususally one of the two beams is allowed to pass through a frequency shifter which will generate an artificial shift in the frequency of that beam. This shift induces a one-dimensional movement of the interference fringes. The velocity of the moving fringes is then either added, if the particle was moving in the same direction, or subtracted, if the particle was moving in the opposite direction. This practice is critical when measuring velocities near zero and in flows where reversals in the flow exist. For more details on LDV measurement principles the reader is referred to Durst et al. (1977).

The light source used in our setup was a Spectra Physics multi-line (457.9-514.5 *nm* wavelength range) 6-*W* Argon-ion laser operating in TEM00 mode or Gaussian beam intensity profile (Figure 4.3). Transmitting optics were used to condition the beams and guide them into the fiber optic cables and, in turn, into the fiber optic probe. A frequency shift unit was used on each component to resolve the directional ambiguity in the flow. The four collimated beams, two for each component, were focused at a point in the flow field where measurements were made. The scattered light was collected using the receiving optics, separated using a multicolor receiver and guided into the blue and green channels. Signals were detected via a photo-multiplier tube (PMT) which converted the received light into electrical current. A signal conditioning processor amplified the detected signal and sent the analog signal to a down-mixing unit within the frequency shifter electronic module. The down-mixing process reduced the actual frequency shift from 40 *MHz* to either 0.002, 0.005, 0.01, 0.02, 0.05, 0.1, 0.2, 0.5, 1, 2, 5, or 10 *MHz*. The last step in the signal conditioning process used high-pass and low-pass frequency filtering to eliminate all frequencies that did not lie within a preselected range.

Signal processing was performed by an IFA-750 Digital Burst Correlator© (TSI, Inc.) to process the LDV signals. It received signals from the down mixing unit in the form of electrical signals, and from these it extracted velocity information. An oscilloscope was used to provide a visual display and a continuous monitoring of the Doppler burst throughout the experiment. Most signal processing parameters such as filtering range, SNR level etc., were software controlled. The FIND© software (TSI, Inc.) also controlled the traversing system where the desired sampling locations were stored in a file. During the sampling process these positions were recalled and then the probe was automatically moved from one position to the other until the measurement campaign was over. The traverse system provided position uncertainties smaller than $\pm 10\ \mu m$.

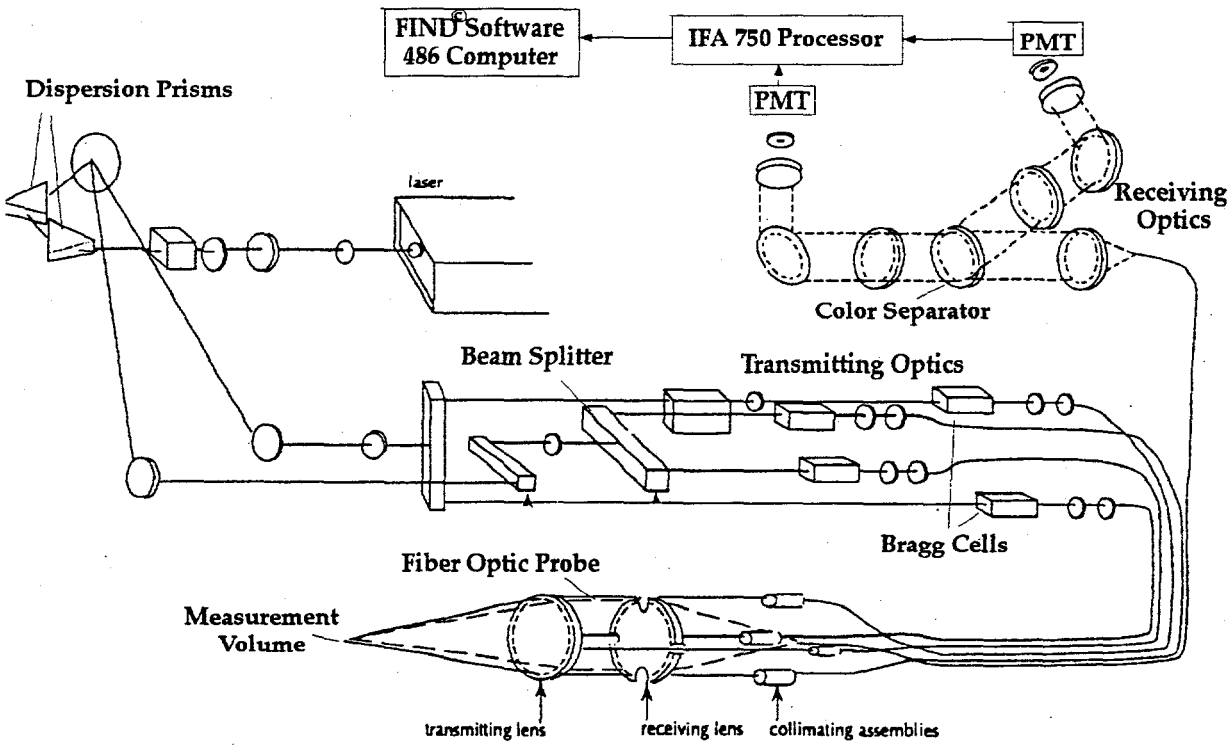

Figure 4.3. Schematic Drawing of the LDV System used for Turbulence Measurements.

Data analysis followed again using the FIND© software, which also displayed detailed information (velocity or frequency histograms) and created text files where statistical as well as sampling control parameters were stored along with the corresponding data locations. The time-averaged and turbulent quantities were determined from the experimental data based on the following equations:

Time-Averaged: $$U \equiv \bar{u} = \frac{1}{T} \int u(t)dt \tag{4.3}$$

Turbulent Intensity: $$u' = \{\sum (U - u)^2\}^{1/2} \tag{4.4}$$

In the above equations, T is the total burst time and u is the instantaneous velocity detected during each burst period:

$$u = d_f \cdot \left(\frac{N}{T} * 1000 - f_s\right) \tag{4.5}$$

where N is the number of cycles, T is the time for N cycles (in nanoseconds), and f_s is the frequency shift in *MHz*.

4.2 Experimental Setup

The test facility for these experiments was designed and built to remotely and non-intrusively study the flow field of submerged turbulent jets. The facility was comprised of a closed flow loop, a seeding system, a fully automated 3-D traverse system, an optical diagnostic system, and a rheometer (to be used in the rheological characterization of the test fluids). The design of the flow loop and the test-section is flexible enough to accommodate a wide variety of single-phase Newtonian, single-phase non-Newtonian, or two-phase (suspension of solids in Newtonian/non-Newtonian fluid) fluids. In addition, different optically-based measurement techniques could be used such as laser sheet visualizations, laser Doppler velocimetry (LDV), or a global planar flow field measurement technique like particle image velocimetry (PIV).

Figure 4.4 is a schematic drawing of the flow loop which consists of a 122 *cm* (48 *in*) long by 46 *cm* (18 *in*) rectangular test section made of clear cast acrylic, a 1/2 *hp* Moyno progressing cavity pump (4.4 *gpm* at 50 *psi*), a 90 *VDC* (5.1 *amp*) variable speed DC motor, DC motor controller (0-90 *VDC*), positive-displacement flowmeter, a nozzle assembly (S.S. and brass), trapped air reservoir, 2.5 *cm* (1 *in*) nominal diameter inter-connecting pipe (PVC), and the data acquisition system. Hydraulic surges in the system are prevented by using an air trapped reservoir in combination with an open system. The pressure inside the test section is bounded by the hydrostatic pressure head. All materials are maintained near ambient temperature.

To create a flow geometry which can be easily simulated with the computational codes, we placed four curved baffels longitudinally along the corners of the test section, as shown in the cross-sectional view of Figure 4.5. This arrangement provided a nearly circular cross-section without blocking the path of the LDV beams.

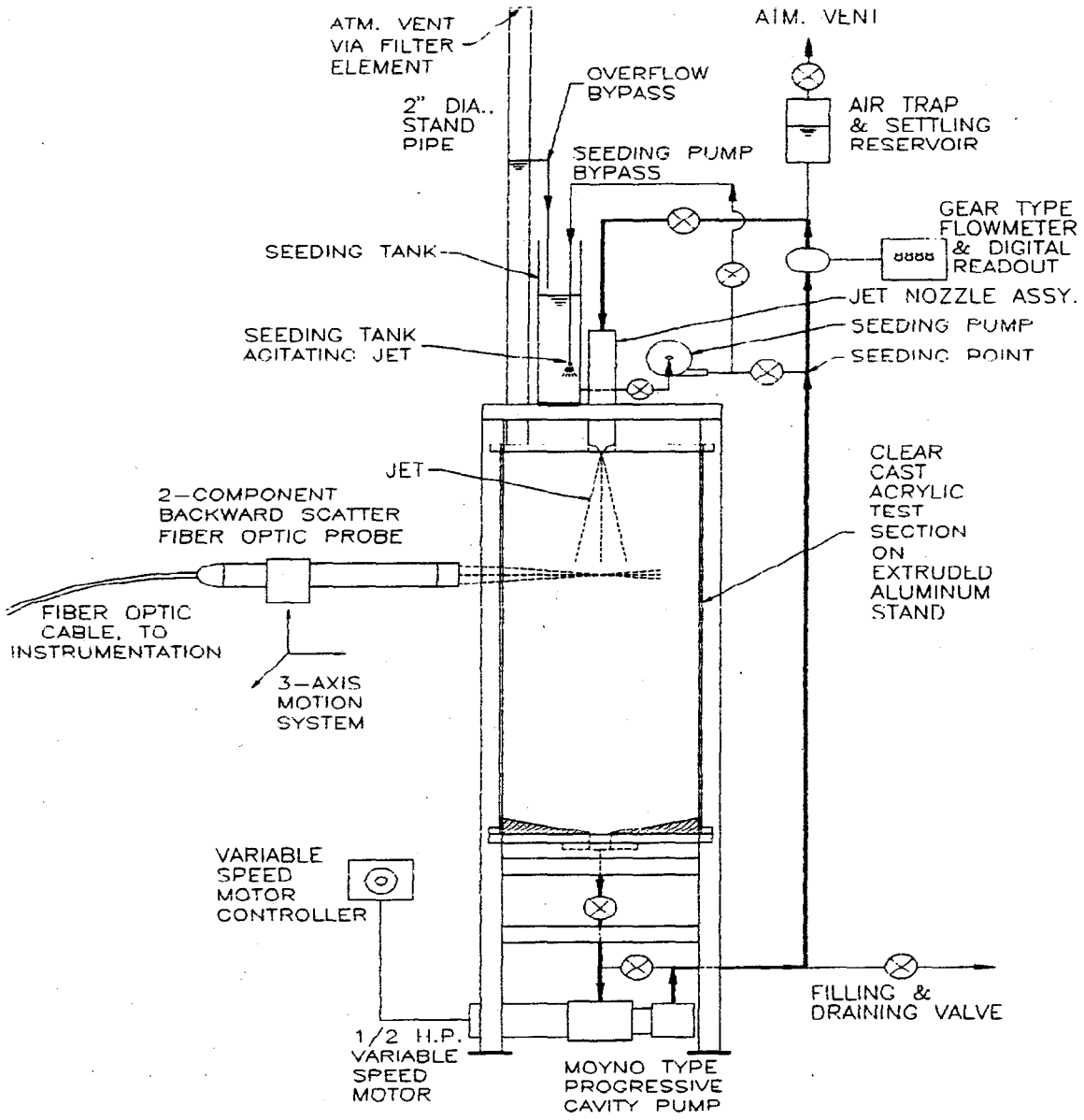

Figure 4.4. Schematic Drawing of the Flow Loop for Jet Turbulence Measurements

A Moyno type progressive cavity pump was selected for these experiments to minimize the pump generated vibrations travelling through the fluid or the test section. Such vibration could give rise to biased error in the measurement of turbulent intensity. A gear type, positive displacement flow meter was selected because it provides a more direct measurement of the flow rate which is especially suitable when using slurries and yield fluids. The flow meter was carefully calibrated throughout the range of measurement using a standard stop watch and volume measurements technique.

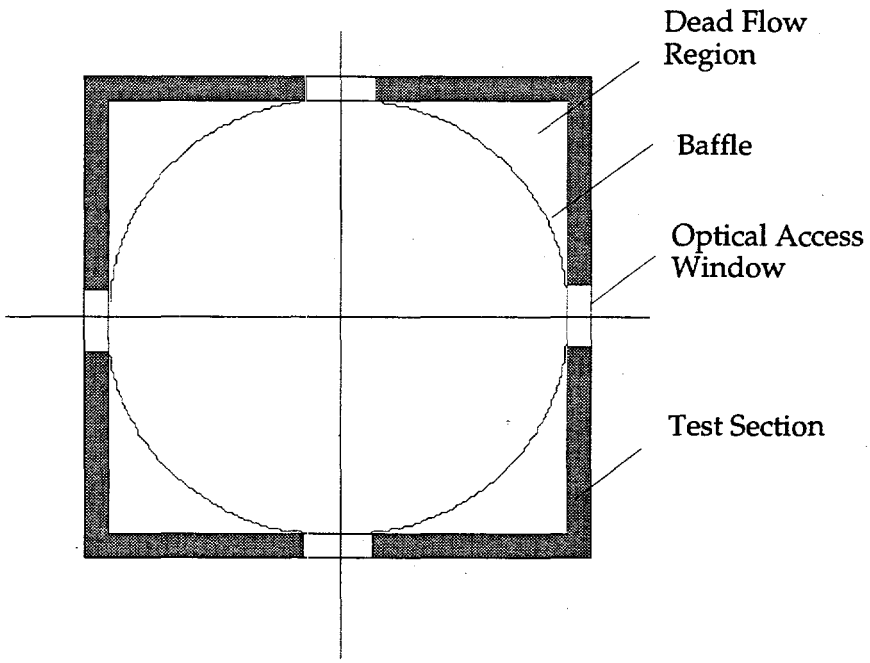

Figure 4.5. Schematic Drawing of the Cross-Section of the Test Vessel for Jet Turbulence Measurements

4.3 Test Fluids and Their Rheology

In order to predict and explain the behavior of non-Newtonian fluids in any complex flow, it is important to isolate certain properties of the non-Newtonian fluids by using a specific constitutive rheological model. As mentioned before, one important characteristic of the radioactive waste is shear-thinning. Therefore, the initial investigation concentrated on how a shear-thinning rheology affects the submerged turbulent jet characteristics as opposed to the baseline Newtonian fluid.

Rheological characterization of non-Newtonian fluids are in general carried out using a narrow-gap concentric cylinder rotational rheometer. This particular geometry is suitable since it is a simple shear or viscometric flow in which a steady-state shear flow is generated by two cylinders moving relative to each other at a constant linear speed, U, in a direction parallel to each other.

In general, for a time-independent and purely-viscous non-Newtonian fluid, the deviatoric stress tensor, τ_{ij}, can be related to the rate-of-deformation tensor, D_{ij}, via the following generalized relationship:

$$\tau_{ij} = -\eta D_{ij} \tag{4.6}$$

where η is the apparent or effective viscosity of the fluid. In a simple shear flow between two parallel plates, the previous relation is simplified as follows:

$$\tau = -\eta \dot{\gamma}. \tag{4.7}$$

In Equation (4.7) $\dot{\gamma}$ is the only nonzero component of the rate-of-deformation tensor and is the ratio of the velocity difference to the distance or gap between the two cylinders.

The curve generated when plotting the shear-stress, τ, versus the shear-rate, $\dot{\gamma}$, is referred to as the rheogram or flow curve. Another representation of the rheological characteristics is the apparent or effective viscosity, η, as a function of shear-rate. For non-Newtonian fluids the simplest and most commonly used phenomenological model describing a shear-rate dependent viscosity is the two-parameter power-law or Ostwald-de Waele model.

$$\tau = K \dot{\gamma}^n \tag{4.8}$$

where K is the consistency factor and n is the power-law or behavior index of the fluid. The asymptotes of the power-law model are: 1) n=1, Newtonian behavior, and 2) n=0, which results in a plastic like behavior. If n>1 then the material is shear-thickening, and if n<1 the material is shear-thinning. We will not be concerned about shear-thickening fluids and will focus our attention to fluids where $n \leq 1$. The apparent viscosity of a power-law non-Newtonian fluid is defined by substituting Equation (4.7) into (4.8) and solving for η.

$$\eta = K \dot{\gamma}^{n-1}. \tag{4.9}$$

An extension of the power-law type fluids are fluids that have, in addition to shear-thinning behavior, a yield prior to flow, similar to the sludges in the tanks. A constitutive model representating the behavior of such fluids is referred to as the Herschel-Bulkley model.

$$\tau = \tau_o + K \dot{\gamma}^n \tag{4.10}$$

where τ_0 is the yield stress of the material. Although we have argued that the sludges have yield stress (or strength of different kind), the supernatant liquid during mixing may be non-Newtonian and not have a yield stress (i.e., a power-law fluid). Although we are interested in turbulence within a high Reynolds number jet submerged in a yield fluid, we have already presented some results from our previous work, and we will limit the current section to experiments on turbulence of power-law fluids. Further yield stress fluid studies are planned for the near future.

The non-Newtonian fluid used and characterized in these experiments was an aqueous Carbopol™ solution. It was prepared by dispersing 500 *ppm* (by weight) of EZ-1 Carbopol resin in deionized water. A Paar Physica Rheolab MC1 rotational rheometer system was used for the characterization of the fluid. This instrument is a controlled-stress rheometer which provides a more direct and to a smaller degree of uncertainty measurement of the yield stress.

Figure 4.6 (a) is a rheogram of this solution. Note that the data points for the increasing and decreasing shear rate fall on top of each other suggesting that there was no hysteresis or time-dependent behavior. This feature is quite attractive since it limits the degrees of freedom in the problem for a more conclusive explanation of the observations and results. As shown on the figure, a power-law model fit the data very closely, with n=0.69 and K=0.115, within approximately four orders of magnitude of the shear rate tested. Figure 4.6 (b) is the apparent viscosity of the fluid as a function of shear rate. The apparent viscosity was determined by applying Equation (4.9) to the results shown in Figure 4.6 (a). Note that the viscosity reaches asymptotic limits for both low shear rates ($<10^1$) and high shear rates ($>5\text{x}10^3$). This type of behavior is usually modeled using the Carreau constitutive model.

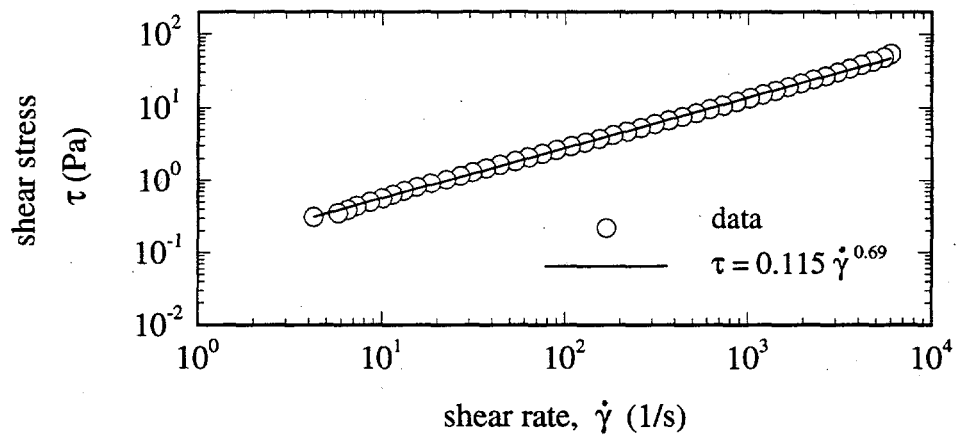

(a) Shear Stress vs. Shear Rate

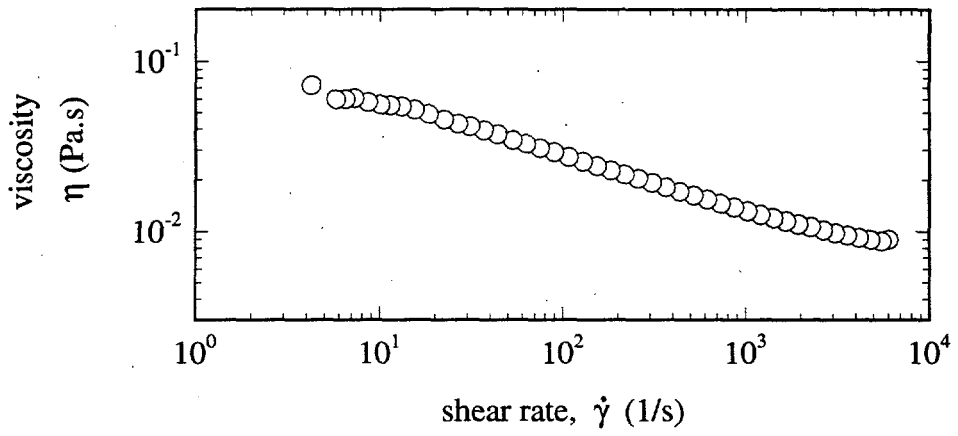

(b) Viscosity vs. Shear Rate

Figure 4.6. (a) Rheogram of the Non-Newtonian Solution Used in the Tests; (b) Apparent Viscosity vs. Shear Rate Curve.

4.4. Test Matrix

These measurements are aimed at investigating the effects of the shear-thinning index, n, and the Reynolds number on the turbulence within the jet. For a power-law fluid the following definition for the Reynolds number is adopted and used.

$$Re \equiv \frac{\rho D^n U_j^{2-n}}{8^{n-1} K}, \tag{4.11}$$

where, D is the nozzle diameter and U_j is the jet velocity at the nozzle exit.

Table 4.1. Newtonian Fluid Tests

Flow Rate *(lpm)*	**Jet Velocity** U_j *(m/s)*	***K*** *(Pa.s^n)*	***n***	**Reynolds Number**
2.45	1.23	0.0008	1	10,000
4.90	2.46	-	-	20,000
7.35	3.69	-	-	30,000
9.80	4.92	-	-	40,000
12.3	6.15	-	-	50,000
14.7	7.38	-	-	60,000
17.2	8.62	-	-	70,000
19.6	9.85	-	-	80,000
22.1	11.08	-	-	90,000
24.5	12.31	-	-	100,000

Table 4.2. Non-Newtonian Fluid Tests

Flow Rate *(lpm)*	**Jet Velocity** U_j *(m/s)*	K $(Pa.s^n)$	n	**Reynolds Number**
5.69	2.86	0.115	0.69	2,000
7.75	3.89	-	-	3,000
9.66	4.85	-	-	4,000
11.5	5.75	-	-	5,000
13.2	6.61	-	-	6,000
14.8	7.44	-	-	7,000
16.4	8.24	-	-	8,000
18.0	9.02	-	-	9,000
19.5	9.77	-	-	10,000
22.4	11.23	-	-	12,000
25.2	12.64	-	-	14,000
27.9	14.00	-	-	16,000
30.5	15.32	-	-	18,000
33.1	16.60	-	-	20,000
38.4	19.29	-	-	24,335

4.5 Results

Figure 4.7 includes two time history plots of the velocity measured with the LDV system within the Newtonian and the non-Newtonian fluids at two different axial locations. These plots are real-time trances that were analyzed to produce the velocity statistics as described in Section 4.2. The time history of the velocity is converted into histograms or probability density function, as shown in Figure 4.8. The mean or time-averaged velocity and standard deviation or turbulent intensity is then calculated from the prbability density function of velocity.

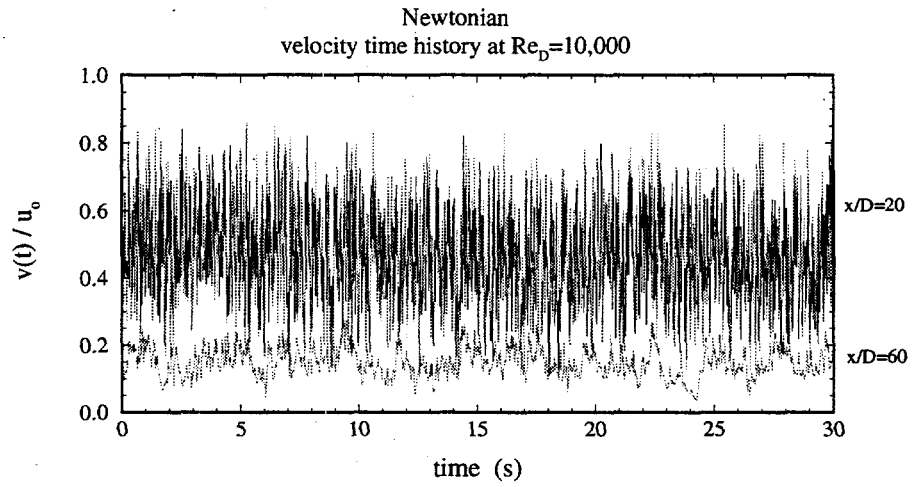

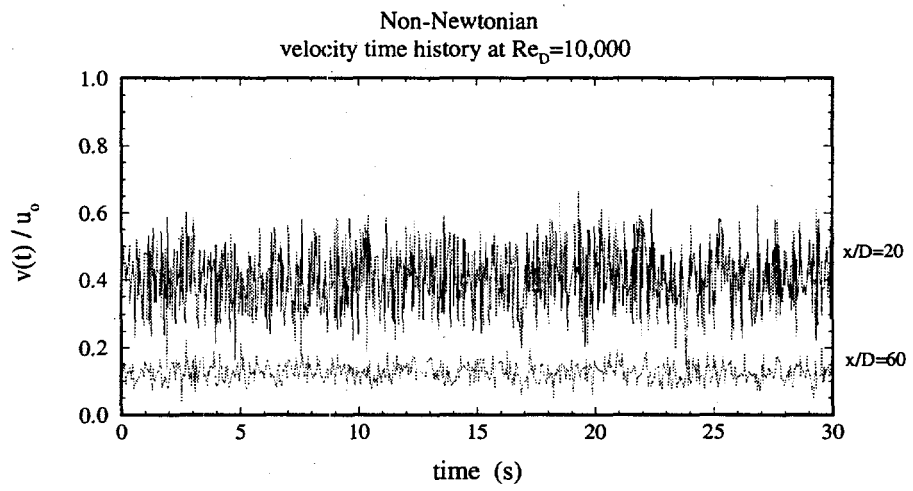

Figure 4.7. Sample Real-Time Plots of the Velocity in the Turbulent Newtonian and Non-Newtonian Jets.

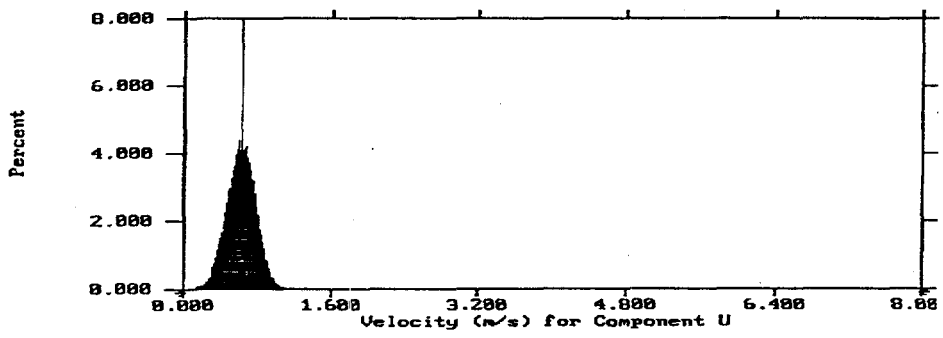

Figure 4.8. A Sample Probability Density Function of Velocity.

As mentioned before, we would like to know the functional dependence of the mean flow and turbulent intensity within the jet on the flow geometry and dynamics. Figure 4.9 is the inverse of the dimensionless centerline velocity of the Newtonian jet in the streamwise or axial direction, *x/D*. Four different flows with Reynolds numbers ranging between 10,000 and 70,000 were studied for these set of measurements. The solid line is the best fit data for Reynolds number of 10,000 data. Note that almost all the measurements for $x/D<60$ agreed very closely with the solid line plot. The equation that seemed to fit the *Re*=10,000 data followed the format shown below:

$$\text{Newtonian:} \quad u_c / U_o = \frac{7.69}{(x/D - 3.3)}. \tag{4.12}$$

Beyond $x/D>60$, the centerline velocity becomes more scattered but the mean behavior tends toward the more commonly used correlation for the jet, $u_c / U_o = 6.3/(x/D)$. So we believe that the rate of centerline decay for a jet within an enclosure is not as rapid as commonly believed. This difference may be attributed to the strong recirculation that exists in the corner of the tank, as conceptually shown in Figure 2.4. Similar measurements for the non-Newtonian jet, as shown in Figure 4.10, reveal that the centerline velocity decay follows the best fit equation shown below:

$$\text{Non-Newtonian:} \quad u_c / U_o = \frac{6.31}{(x/D - 5.2)}. \tag{4.13}$$

This equation suggests that the centerline velocity in the non-Newtonian jet (of particular rheology studied here) within an enclosure is not greatly influenced by the recirculating flow and it is close to what is commonly reported for a turbulent Newtonian jet. Thus we conclude that for pseudoplastic jets where $n \geq 0.69$, the centerline velocity does not deviate greatly from the Newtonian jets. However, later in this section we will show that this condition is satisfied only if the Reynolds number is larger than ~20,000.

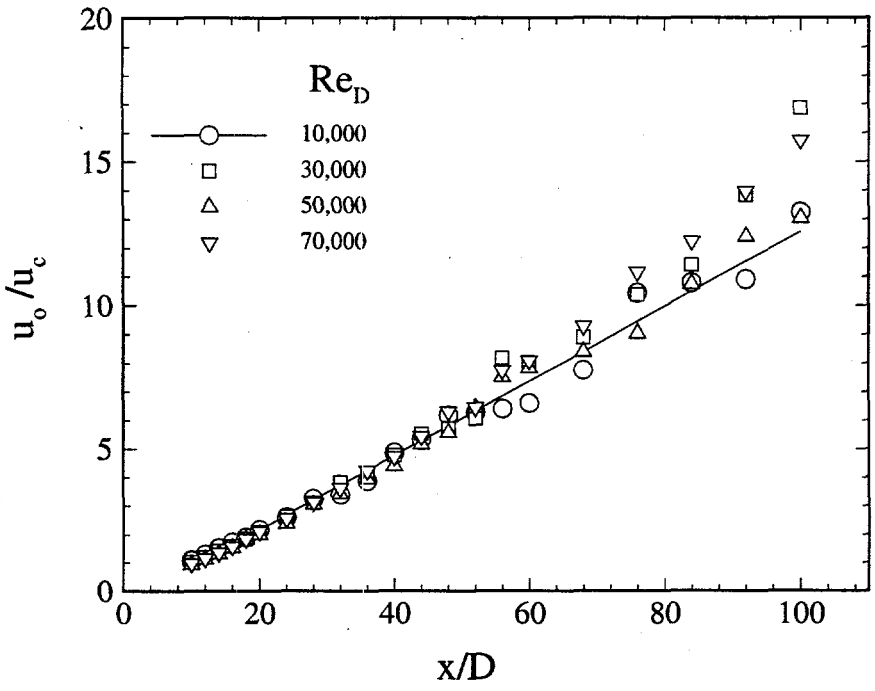

Figure 4.9. Time-Averaged Centerline Velocity Development in the Axial Direction for the *Newtonian* Jet.

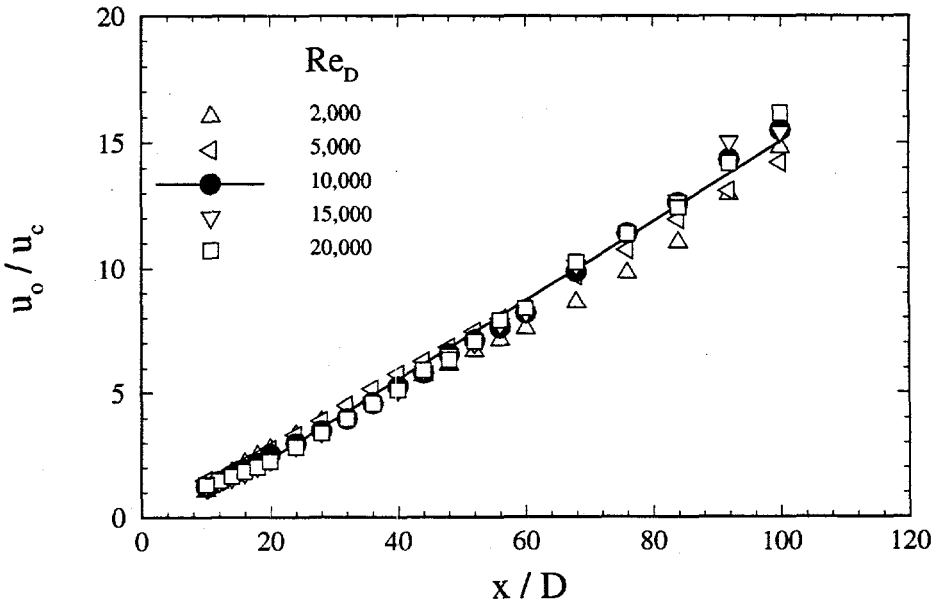

Figure 4.10. Time-Averaged Centerline Velocity Development in the Axial Direction for the *Non-Newtonian* Jet.

Figure 4.11 is the distribution of the dimensionless turbulent intensity, u'/U_o, along the centerline of the Newtonian jet. In each case, the turbulent intensity, u', is normalized by the nozzle exit velocity, U_o, at the particular Reynolds number studied. The various flow conditions appear to produce extremely similar and repeatable values. The best fit curve shown on the figure has a form as shown below

$$\text{Newtonian:} \quad u_c'/U_o = 2.5/(x/D). \tag{4.14}$$

This data is consistent with the results of Wygnanski and Fiedler (1969) for a turbulent free jet. Similar results for the non-Newtonian jet, as shown in Figure 4.12, produces the following best fit curve:

$$\text{Non-Newtonian:} \quad u_c'/U_o = 1.8/(x/D). \tag{4.15}$$

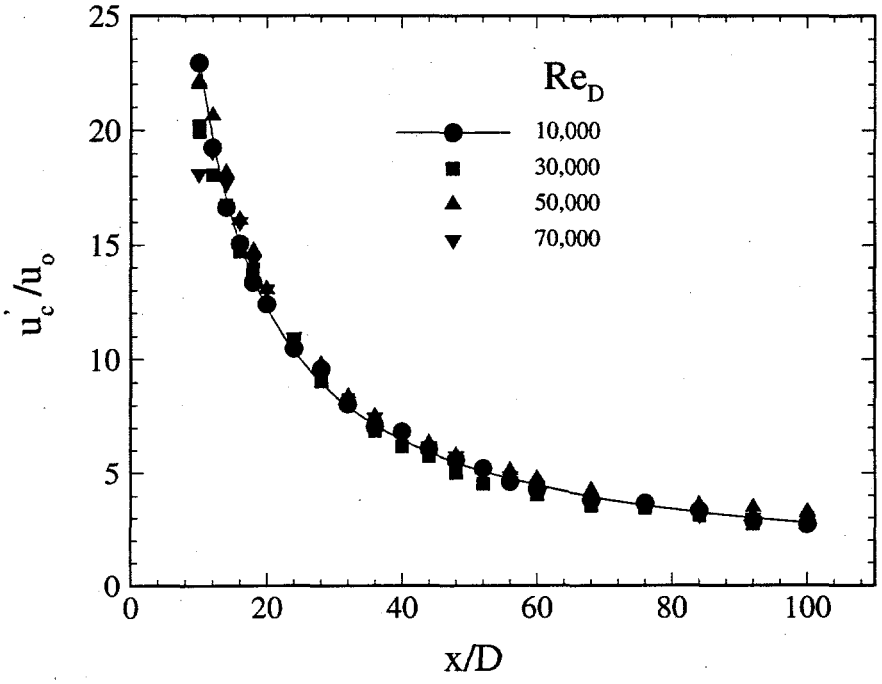

Figure 4.11. Centerline Turbulent Intensity Development in the Axial Direction for the *Newtonian* Jet.

An illuminating approach of looking at our data is the plot of u'/u_c as a function x/D. When we divide Equations (4.12) and (4.13) by (4.14) and (4.15), respectively, we obtain the following relations:

$$\text{Newtonian:} \quad u_c'/u_c \approx 0.4 * (1 - \tfrac{10}{x/D}), \qquad x/D>50 \tag{4.16}$$

$$\text{Non-Newtonian:} \quad u_c'/u_c \approx 0.29 * (1 - \tfrac{5.2}{x/D}), \quad x/D>10. \tag{4.17}$$

The above relations suggest that as $x/D \to \infty$, or at the asymptotic limits, the ratios of u'/u_c reach 0.4 and 0.29 for the Newtonian and non-Newtonian jets, respectively. Thus, the turbulent intensity in the non-Newtonian jet is found to be approximately 28% smaller than the Newtonian jet. Referring to the results for a *free* jet reported in the literature (e.g., Wygnanski and Fiedler 1969), we find that the asymptotic limit of u'/u_c for a turbulent Newtonian free jet is ~0.29. Therefore, our data suggests that the Newtonian jet turbulence within the enclosure (the confined jet) is approximately 28% higher than a *free* jet. The results of our analysis presented in Figure 2.6 predicted that for an enclosure the size of our tank (L=127 *cm* and R=25 *cm*, and L/R=5), the TKE should have been 23% higher. This translates into approximately 48% higher turbulent intensity, which is about twice what we measured. We consider these results very close, in that both the model and the data were able to find a higher turbulent intensity for the Newtonian case.

In Section 2.4 we argued that the recirculating flow for a shear-thinning or pseudoplastic fluid will be much more viscous and as a result we do not expect the turbulence feedback to be significant. Our data confirms that the turbulence level obtained within the non-Newtonian fluid is approximately the same as what is reported for a turbulent *Newtonian free jet*.

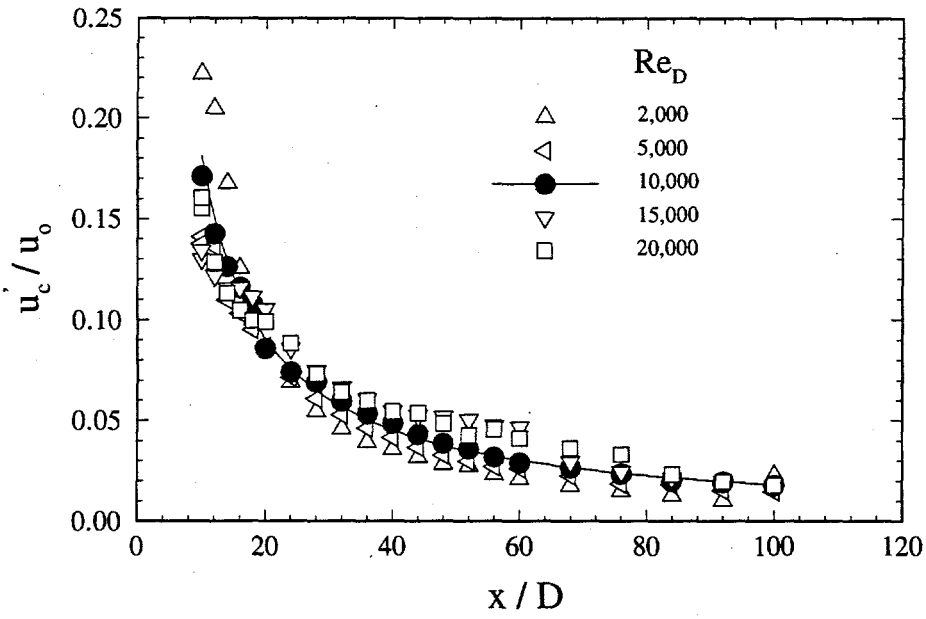

Figure 4.12. Centerline Turbulent Intensity Development in the Axial Direction for the *Non-Newtonian* Jet.

The results shown in Figures 4.9 through 4.12 demonstrate that although the mean or time-averaged centerline velocities are approximately the same for both Newtonian and non-Newtonian jets, the turbulent intensities are different. It is therefore of interest at this point to investigate whether or not these two quantities ever become independent of rheology as the Reynolds number changes. In the next set of tests, therefore, we investigated how the Reynolds number affects the turbulence in the jets for both Newtonian and non-Newtonian fluids.

Figures 4.13 and 4.14 show the variation of the dimensionless time-averaged velocity and turbulent intensity along the centerline of the Newtonian jet as a function of Reynolds number. These measurements were made at three different axial locations and cover a wide range of Reynolds number between 10^4 and 10^5. The data shows some scatter at x/D=60 for some unknown reason. However, the overall trend manifests a lack of dependence of the mean and standard deviation of velocity on the Reynolds number when the samples are sufficiently large to reach statistically stationary conditions. This is a significant finding and one that confirms the results of the analysis provided in Section 2.4. Recall that the model developed for turbulence in a confined jet predicted, against our intuition, that there is no dependence on the Reynolds number. The data confirm the result of predictions.

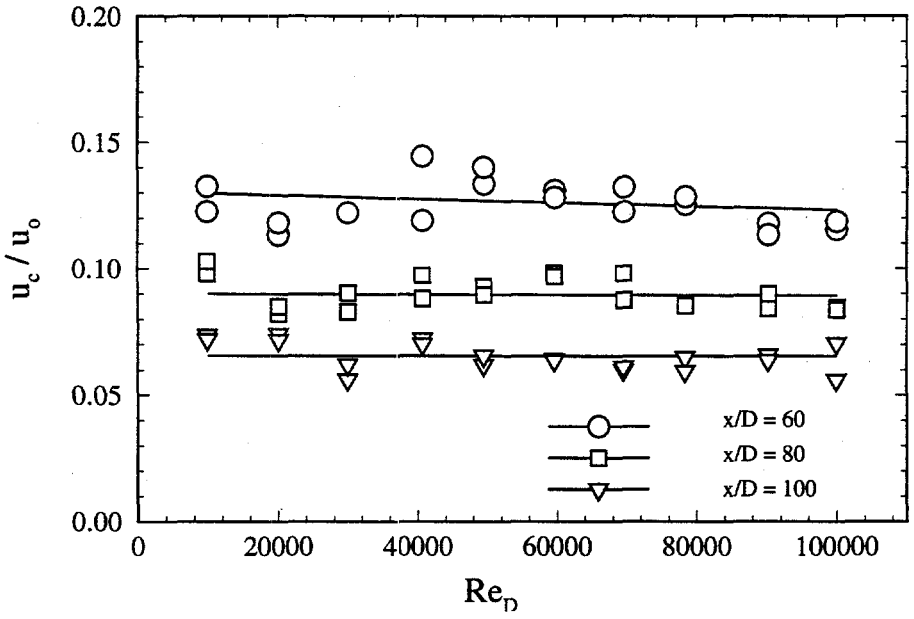

Figure 4.13. Dimensionless Time-Averaged Centerline Velocity for the *Newtonian* Jet as a Function of Reynolds Number.

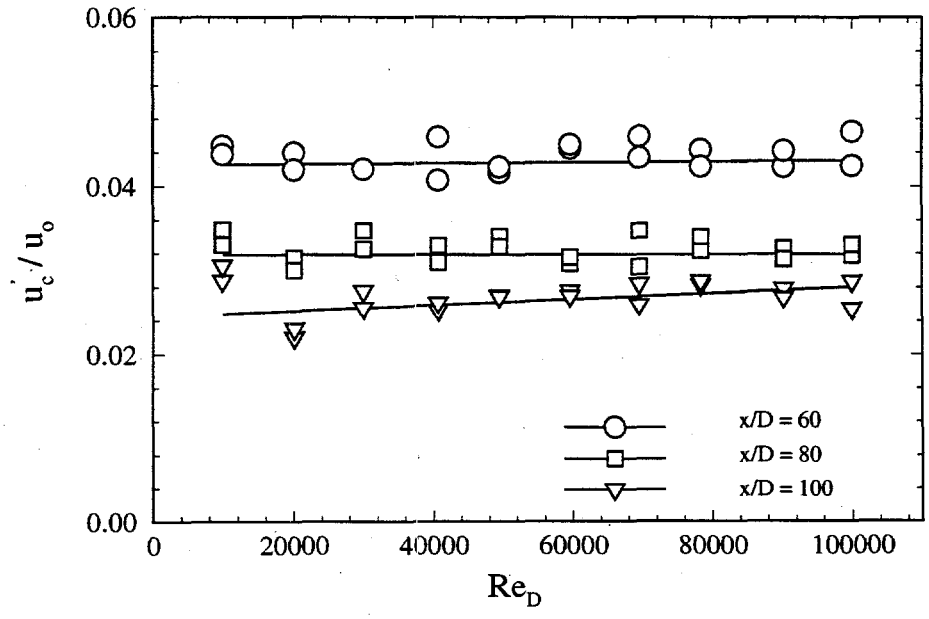

Figure 4.14. Dimensionless Centerline Turbulent Intensity for the *Newtonian* Jet as a Function of Reynolds Number.

What about the non-Newtonian jet? We refer to the results shown in Figures 4.15 and 4.16. Clearly, the data reveal that both the time-averaged velocity and the turbulent intensity depend on the Reynolds number. The change observed in the turbulent intensity at x/D=60 from Re_D=2000 to 20,000 is approximately 35%. However, these figures also show that these parameters are becoming less and less dependent on the Reynolds number as Re_D becomes large. Unfortunately, because the non-Newtonian fluid used had a higher viscosity than water (Newtonian tests), the pump was not able to produce higher flow rates than ~10.1 gpm to obtain higher Reynolds numbers.[13] Conversely, the low flow rates could not be reliably controlled for the Newtonian tests to obtain Reynolds numbers smaller than 10,000. Careful examination of the non-Newtonian data shows that beyond a Reynolds number of 10,000 not only does the velocity characteristics become independent of the Reynolds number, but also the asymptotic conditions closely agree with the Newtonian free jet values reported in the literature (see Wygnanski and Fiedler 1969).

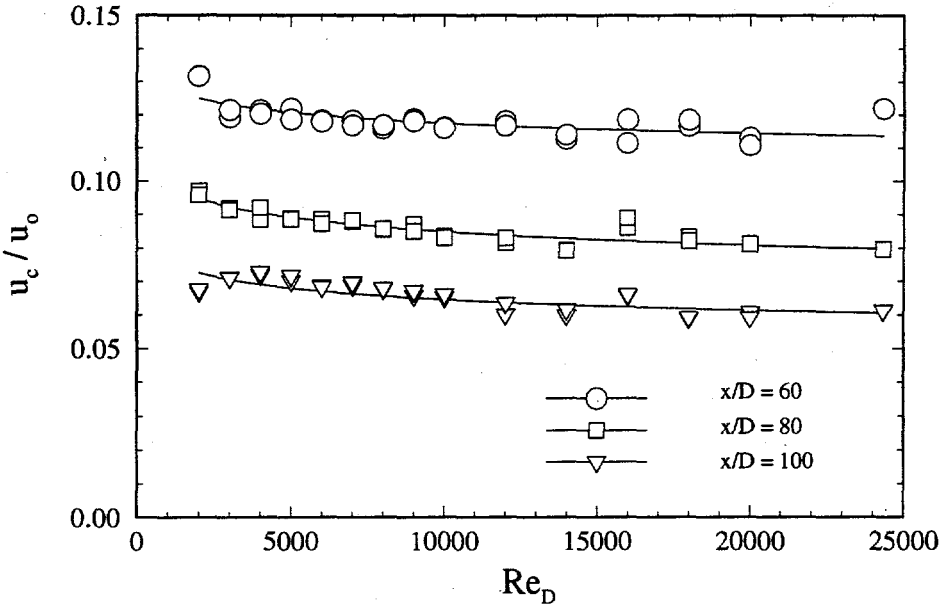

Figure 4.15. Dimensionless Time-Averaged Centerline Velocity for the *Non-Newtonian* Jet as a Function of Reynolds Number.

[13] Even at the highest flow rate of 10.1 *gpm*, producing a nozzle exit velocity of 19.3 *m/s* and shear rates exceeding 3000 *1/s*, the viscosity was 10 times higher than water (see Figure 4.6).

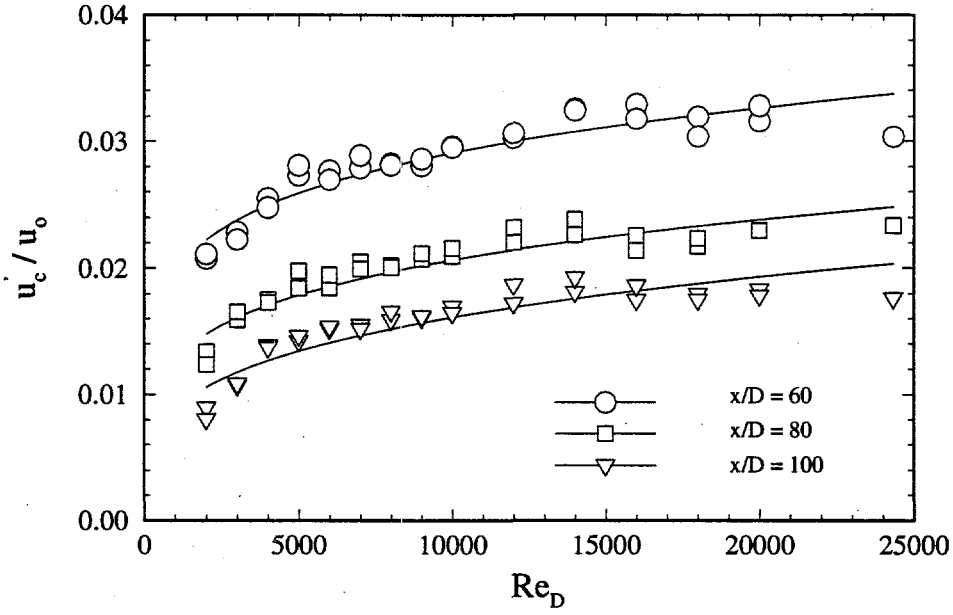

Figure 4.16. Dimensionless Centerline Turbulent Intensity for the *Non-Newtonian* Jet as a Function of Reynolds Number.

We measured the velocity profile across the non-Newtonian jet at several axial positions of x/D=10, 15, 20, 25, and 30. We nondimensionalized the velocity and radial positions with the centerline velocity of the jet and axial position, respectively. The resulting profiles of the time-averaged velocity and the turbulent intensity profiles are shown in Figures 4.17 and 4.18. The velocity profiles appear to be fully similar as is usually observed in a Newtonian jet. This similarity reveals that, unlike what we observed for the yield pseudoplastic fluid in Figure 2.8, the momentum flux in a pseudoplastic (no yield stress) fluid is preserved. Therefore, we can argue that the fluid has to have a true yield in order for the momentum flux to drop in the axial direction, as shown in Equations (2.19) and (2.21). Otherwise, the momentum is conserved in the axial direction. Based on all these observations, we then conclude that our non-Newtonian jet has become fully-developed and self-similar beyond a Reynolds number of 10,000 and behaves just like a turbulent Newtonian free jet.

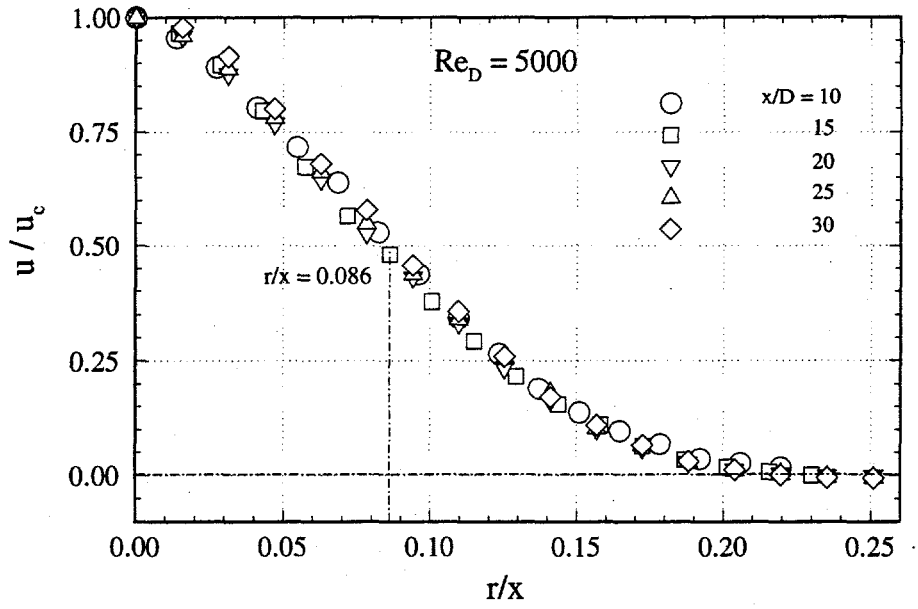

Figure 4.17. Dimensionless Time-Averaged Velocity Profile for the *Non-Newtonian* Jet.

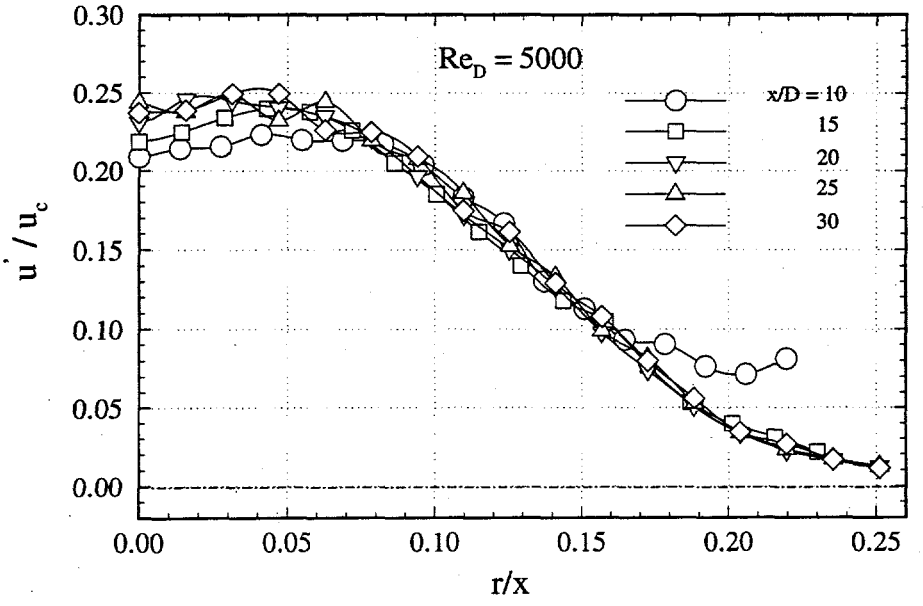

Figure 4.18. Dimensionless Turbulent Intensity Profile for the *Non-Newtonian* Jet.

5.0 Discussion of Results and Conclusions

In this report we have examined some of the fundamental mechanisms expected to be at work during mobilization of the waste within the double-shell tanks at Hanford. The motivation stems from the idea that in order to properly apply correlations derived from scaled tests, one would have to ensure that appropriate scaling laws are utilized. Further, in the process of delineating the controlling mechanism during mobilization, we are validating and strengthening the currently used computational codes based on our findings.

As a first step, we performed experiments at 1/50-scale, which is different from what had been performed in the previous fiscal years (i.e., 1/12- and 1/25-scale). We speculated that if the current empirical correlations are to work, they should be scale invariant. A total of eleven tests were performed at this scale. Once suspect data were eliminated, our results showed that linear scaling between the 1/25-scale and 1/50-scale correlations do not work well. We examined several mechanisms in the scaled tests which might have contributed to the discrepancies between the results at these two scales. We were unable to find any deficiencies in the experimental approach and most of the data. Cognizant of these results, we concluded that the use of the current empirical correlations for ECR should be done cautiously. Also, we suggested that the appropriate properties of the material for yielding should be used in the correlations.

To better understand some of the fundamental mechanisms within the "separate-effect" processes during mobilization, we carried out some theoretical analysis and performed supporting laboratory experiments. The theoretical analysis revealed the following results:

- Erosion forces for a Newtonian jet do not depend on the Reynolds number if the jet - sludge interaction takes place in a normal incidence mode. On the other hand, if the mode of interaction between the jet and sludge is off-normal[14] then the erosion forces become dependent on Reynolds number. The impact of this finding is that if you do not match the Reynolds number at different scales while the sludge is being eroded by an off-normal jet impact, then the different scales will likely not yield *similar* results.

---

[14] That is, anywhere between parallel interaction and normal interaction but not including normal incidence.

- The turbulence in the jet placed within an enclosure depends on the enclosure geometry but does not depend on the enclosure or jet Reynolds numbers. The impetus behind such analysis was to evaluate whether or not the turbulence level within a jet at the smaller scales was higher and as a result leads to higher erosion forces. The experiments performed in the laboratory using controlled conditions and a well-suited measurement technique of laser-Doppler velocimetry confirmed our hypothesis that the turbulence level in the jet is independent of Reynolds number. For both Newtonian and non-Newtonian fluids used in these tests, a minimum Reynolds number of 10,000 was required before the turbulence approached an asymptotic condition within our measurement uncertainty (which was less than ±5%).

- The geometrical dependence predicted from the model appears in the form of L/R where L is the length of the jet and R is the diameter of the tank in which the jet is submerged. At L/R =5, which is the geometry of the test section in our experiments, we obtained approximately 28% higher turbulent intensity for the confined jet over the free jet turbulence. This is in qualitative agreement with the results of analysis provided in Section 2.4. However, we did not perform experiments at other L/R ratios to further verify our model. The impact of this set of results is that as long as the ratio of L/R over different scales is not changed, which is the premise behind geometric scaling, then the turbulent intensity in the jet will remain the same. Therefore, we don't believe that turbulence for the Newtonian jet plays a role in proper scaling of the correlations.

- Consistent with the model and our intuition, the turbulence feedback was not significant when the recirculation flow became more viscous for a non-Newtonian fluid. As a result, the turbulence obtained within the non-Newtonian fluid was approximately the same as a Newtonian free jet, as long as the Reynolds number was higher than 10,000.

- Total momentum flux is not necessarily conserved for a non-Newtonian jet if the fluid in which the jet is submerged has a yield stress. Equation (2.21) suggests that the momentum drop is inversely proportional to the yield stress of the fluid. The impact of such momentum loss is less of an entrainment rate into the jet and as a result less mixing, as well as retardation of the jet. Our data from previous fiscal years confirms this finding (see Figure 2.10). The data presented in Section 4.0 from our current study with a pseudoplastic jet suggests that shear-thinning behavior does not lead to momentum loss, also consistent with our model.

In summary, most of the mechanisms related to scaling of turbulent Newtonian jets and pseudoplastic jets are considered to be unimportant for scaling of the jets. As long as geometric scaling is properly maintained, the fluid does not develop *any* yield stress, and the jet Reynolds numbers are maintained above 10,000, then the dynamics within the jets should scale well. However, we have only studied the jets from a normal jet - sludge interaction point of view. We hypothesize that the reason the 1/50-scale and 1/25-scale (and perhaps 1/12-scale) results do not scale is because of off-normal jet - sludge interaction. We do not believe that the material property variance could play a significant role in the scaled experiments. We fully anticipate that once the effect of off-normal interaction is included, then the results from various scales should collapse onto a unique set of curves. Further, in the interim, the use of the existing empirical correlations in the full scale should be accompanied by the appropriate choice of material properties. The question of what the most suitable properties are is currently being addressed, following from the discussions presented in Section 1.3.

6.0 References

Barchilon, M, and R Curtet. 1964. "Some Details of the Structure of an Axisymmetric Confined Jet with Back Flow." *ASME Fluids Eng. Conf.*, 64-FE-23:1-17.

Barker, SJ. 1973. "Laser-Doppler Measurements on a Round Turbulent Jet in Dilute Polymer Solutions." *J. Fluid Mech.*, 60.

Beltaos, S, and N Rajaratnam. 1974. "Impinging Circular Turbulent Jets." *Proc. ASCE, J. Hydraul. Div.*, 100:1313-1328.

Beris, AN, JA Tsamopoulos, RC Armstrong, and RA Brown. 1985. "Creeping Motion of a Sphere through a Bingham Plastic." *J. Fluid Mech*, 158: 219-244.

Bird, RB, RC Armstrong, and O Hassager. 1977. "Dynamics of Polymeric Liquids." Vol. 1, Wiley, New York.

Channell, GM and CF Zukoski. 1997. "Shear and Compressive Rheology of Aggregated Alumina Suspensions." *AIChE J.*, Vol. 43, No. 7, pp. 1700-1708.

Churnetski, B. V. 1982. "Prediction of Centrifugal Pump Cleaning Ability in Waste Sludge." *Nuclear and Chemical Waste Management.* v. 3, pp. 199-203.

Curtet, R, and FP Ricou. 1964. "On the Tendency to Self-Preservation in Axisymmetric Ducted Jets." *ASME Fluids Eng. Conf.*, 64-FE-20:1-11.

DiCenso, AT, LC Amato, and WI Winters. 1995. *Tank Characterization Report for Double-Shell Tank 241-SY-102.* WHC-SD-WM-ER-366 Rev. 0, Westinghouse Hanford Company, Richland, Washington.

Douillard, GR. 1995. "Time-Averaged Measurements of The Velocity Field of a Pseudoplastic Free Jet." Master's Thesis, Washington State University, Pullman, Washington.

Durst, F, A. Melling, and JH Whitelaw. 1977. "Principles and Practice of Laser-Doppler Anemometry." Academic Press.

Fort, JA, JA Bamberger, JM Bates, CW Enderlin, and MR Elmore. 1993. *1/12-Scale Physical Modeling Experiments in Support of Tank 241-SY-101 Hydrogen Mitigation.* PNNL-8476, Pacific Northwest Laboratory, Richland, Washington.

Fosset, H and LE Prosser. 1951. "The Application of Free Jets to the Mixing of Fluids in Bulk." *Trans. Inst. Chem. Engr.*, 29:322.

Fox, EA and VE Gex. 1956. "Single-Phase Blending of Liquids." *AIChE J.*, 2(4): 539-544.

Gutfinger, C and R Shinnar. 1964. "Velocity Distributions in Two-Dimensional Laminar Liquid-into-Liquid Jets in Power-Law Fluids." *AIChE J.*, 10, No. 5.

Hamm, BA, WL West, and GB Tatterson. 1989. "Sludge Suspension in Waste Storage Tanks."

AIChE Journal. v. 35, n. 8., pp. 1391-1394.

Horowitz, J. B. 1980. *One-Twelfth Scale Mock-Up of Tank 16 Cleaning Demonstration.* DPST-80-496. July 31, 1980. Savannah River Laboratory, Aiken, South Carolina.

Jordan, C, GW Rankin, and K Sridhar. 1992. "A Study of Submerged Pseudoplastic Laminar Jets." *J. Non-Newtonian Fluid Mech.*, 41.

Kumar, KR, GW Rankin, and K Sridhar. 1984. "Laminar Length of a Non-Newtonian Fluid Jet." *J. Non-Newtonian Fluid Mech.*, 15.

LaFemina JP. 1995. *Tank Waste Treatment Science Task Quarterly Report for January-March 1995.* PNL-10763, pp 7.1-7.31. Pacific Northwest Laboraotry, Richland, Washington.

McComb, WD. 1990. "The Physics of Fluid Turbulence." Oxford: Clarendon Press.

Meeten, GH. 1994. "Shear and Compressive Yield in the Filteration of Bentonite Suspension." *Colloids Surf. A*, 82, 77.

Mittwally, EM. 1978. "Solutions of Laminar Jet Flow Problems for Non-Newtonian Power-Law Fluids." *J. Fluids Eng.*, 100.

Norwood, KW and AB Metzner. 1960. "Flow Patterns and Mixing Rates in Agitated Vessels." *AIChE J.*, 6(3):432-437.

Onishi Y and JD Hudson. 1996. *Waste Mixing and Diluent Selection for the Planned Retrieval of Hanford Tank 241-SY-102: A Preliminary Assessment.* PNNL-10927, Pacific Northwest National Laboratory, Richland, Washington.

Onishi Y, R Shekarriz, KP Recknagle, PA Smith, J Liu, YL Chen, DR Rector, and JD Hudson. 1996. *Tank SY-102 Waste Retrieval Assessment: Rheological Measurements and Pump Jet Mixing Simulations.* PNNL-1135, Pacific Northwest National Laboratory, Richland, Washington.

Park, JT, RJ Mannheimer, TA Grimley, and TB Morrow. 1989. "Pipe Flow Measurements of a Transparent Non-Newtonian Slurry." *J. Fluids Eng.* Vol. 111, pp. 331-336.

Powell, MR, GR Golcar, CR Hymas, RL McKay. 1995. *Fiscal Year 1993 1/25-Scale Sludge Mobilization Testing.* PNL-10464. Pacific Northwest Laboratory, Richland, Washington.

Powell, MR, CM Gates, CR Hymas, MA Sprecher, and NJ Morter. 1995. *Fiscal Year 1994 1/25-Scale Sludge Mobilization Testing.* PNL-10582. Pacific Northwest Laboratory, Richland, Washington.

Powell, M. R., Y. Onishi, and R. Shekarriz. 1997. *Research on Jet Mixing of Settled Sludges in Nuclear Waste Tanks at Hanford and Other DOE Sites: A Historical Perspective.* PNNL-xxxx, Pacific Northwest National Laboratory, Richland, Washington.

Schlichting, H. 1960. *Boundary-layer Theory.*" McGraw-Hill Book Company, New York, 2nd English Edition.

Serth, RW. 1972. "The Axisymmetric Free Laminar Jet of a Power-Law Fluid." *J. Applied Math. Phys.*, 23.

Shekarriz, A, JR Phillips, and TD Weir. 1995a. "Quantitative Visualization of a Submerged Pseudoplastic Jet Using Particle Image Velocimetry." *J. Fluids Eng.*, Vol. 117, pp. 369-373.

Shekarriz, A, G Douillard, TD Weir, and CD Richards. 1995b. "Rheology and Reynolds Number Effects on the Velocity Field of a Pseudoplastic Jet." *ASME-FED Summer Meeting*, Hilton Head Island, SC, Aug. 13-18.

Shekarriz, A, G Douillard, and CD Richards. 1996. "Velocity Measurements in a Turbulent Non-Newtonian Jet." *J. Fluids Eng.*, Vol. 118, pp. 872-874.

Smith, PA, DR Rector, and A Shekarriz. 1997. "Microstructural and Rheological Characterization of Colloidal Aggregates of Nuclear Waste Slurries." *Int. J. Mineral Processing* (In Press).

Stewart CW, JM Alzheimer, ME Brewster, G Chen, RE Mendoza, HC Reid, CL Shepard, and G Terrones. 1996. *In Situ Rheology and Gas Volume in Hanford Double-Shell Waste Tanks.* PNL-11296, Pacific Northwest Laboratory, Richland, Washington.

Tennekes, H, and JL Lumley. 1992. "A First Course in Turbulence." 4th Reprint, The MIT Press, Cambridge, MA.

Van de Vusse, JG. 1955. "Mixing by Agitation of Miscible Liquids." *Chem. Eng. Sci.*, 4:178-200, Pergamon Press Ltd, London, Great Britain.

White, FM. 1974. "Viscous Fluid Flow." McGraw-Hill Book Company, New York.

White, FM. 1986. "Fluid Mechanics." Second Edition, McGraw-Hill Book Company, New York.

Whorlow, R.W. 1980. Rheological Techniques. John Wiley& Sons, New York.

Wygnanski, I, and H Fiedler. 1969. "Some Measurements in the Self-Preserving Jet." *J. Fluid Mech.*, vol. 38, part 3, pp. 577-612.

Distribution

No. of Copies

Offsite

2 DOE/Office of Scienctific and Technical Information

1 Professor Clyaton Crowe
Department of Mechanical and Materials Eng.
Washington State University
Pullman, Wa 99164

Onsite

2 DOE Richaland Operations

J.J. Davis, S7-53 (2)

Other Hanford Contractors

R.E. Bauer, S7-14
P.W. Gibbons, H6-12
J.W. Lentsch, S2-48
R.P. Marshall, H5-61
C.A. Rieck, S2-48 (3)
J.E. Van Beek, S2-48 (3)
E.W. Leschber, S7-73

Pacific Northwest National Laboratory

J.A. Bamberger, K7-15
J.M. Bates, K7-15
B.C. Bunker, K8-93
E.A. Daymo, P7-19
C.W. Enderlin, K7-15
J.A. Fort, K7-15
G.R. Golcar, P7-20
K.J. Hammad, K7-15
J.P. LeFemina, P7-27
Y. Onishi, K9-33 (5)
M.R. Powell, P7-19
D.R. Rector, K7-15
M.W. Rinker, K5-22
R. Shekarriz, K7-15 (15)
C.W. Stewart, K7-15
D.S. Trent, K7-15
Information Release Office (7)